

**STABILISATION OF IMAGING ACQUISITION TECHNIQUES USING FIELD  
CANCELLATION**

BY

MAX MAHLKE

BACHELOR THESIS IN PHYSICS

submitted to the

FACULTY OF MATHEMATICS, COMPUTER SCIENCE  
AND NATURAL SCIENCES

of the

RWTH AACHEN UNIVERSITY

in

SEPTEMBER 2014

Supervised by

PROF. DR. ACHIM STAHL, III. PHYSIKALISCHES INSTITUT

PROF. DR. VOLKMAR SCHULZ, INSITUTE OF EXPERIMENTAL MOLECULAR IMAGING



## ABSTRACT

---

Magnetic Particle Imaging is a novel medical imaging modality that utilises magnetic fields to measure the local concentration of magnetic nanoparticles. The particle response is superimposed by the exciting magnetic field, rendering the first harmonic in Fourier space non-evaluative with current analog-to-digital converters due to their limited dynamic range. While the use of a band-stop-filter has been successful at removing the first harmonic, the application of a second receive coil in order to diminish the feedthrough interference has been suggested.

This thesis examines a coil topology consisting of a receive coil and a cancellation coil. Simulations are performed to determine error sources and a prototype coil mounting device is used to experimentally verify the approach. A compensation of 55.61 dB is achieved. The arising problem of a phase shift between the induced voltages in the receive and the cancellation coil is addressed with an allpass-filter, increasing the compensation to 66.47 dB. However, the proposed set-up of the allpass-filter decreases the signal-to-noise ratio by three orders-of-magnitude, therefore, the use of a lattice phase equaliser is suggested.



## CONTENTS

---

<b>1</b>	<b>MAGNETIC PARTICLE IMAGING</b>	<b>1</b>
1.1	Principle . . . . .	1
1.2	Coupling Problem . . . . .	5
1.3	State of the Art . . . . .	7
<b>2</b>	<b>INDUCTIVE DECOUPLING</b>	<b>11</b>
2.1	Principle . . . . .	11
2.2	The Scanner . . . . .	12
2.3	Simulations . . . . .	14
2.3.1	Displacement and Distortion Effects . . . . .	14
2.3.2	Electrical Effects . . . . .	19
2.4	Signal-to-Noise Ratio . . . . .	22
2.4.1	Electronic Noise . . . . .	22
2.4.2	Noise Calculation . . . . .	23
2.4.3	Probe Signal . . . . .	24
<b>3</b>	<b>MEASUREMENTS</b>	<b>27</b>
3.1	Feedthrough Interference Measurement . . . . .	27
3.2	The Phase Shift . . . . .	29
3.2.1	Allpass-Filter . . . . .	32
3.2.2	Outlook: Lattice Phase Equaliser . . . . .	37
<b>4</b>	<b>CONCLUSION AND OUTLOOK</b>	<b>39</b>

## LIST OF FIGURES

---

Figure 1	The field lines of the Selection Field, the Drive Field and their superposition for three different phases of the Drive Field to show how the Field Free Point is moved through space. (Taken from [2]) . . . . .	2
Figure 2	Magnetisation behaviour of magnetic nanoparticles as modelled by the Langevin theory. . . . .	3
Figure 3	Helmholtz coil pair generates the Drive Field (grey) and the Selection Field (not pictured) by superimposing an alternating current with a direct current. The Receive Coil (blue) picks up the signal of the magnetic nanoparticles (red). . . . .	4
Figure 4	The induced voltages in the Receive Coil and the amplitudes of their Fourier coefficients. The Drive Field signal (Top) is sinusoidal, while the particles' signal (Middle) resembles spikes due to the non-linearity of the magnetisation behaviour. The Fourier coefficient of the fundamental frequency $f_0$ of the resulting signal (Bottom) is a superposition of the Drive Field and the particles' signal, the higher harmonics solely result from the particles' signal. (Taken from [2]) . . . . .	6
Figure 5	(a) The overall signal (left) is the superimposed feedthrough interference of the Drive Field signal (middle) and the particles' signal (right). The interference is several orders of magnitude higher than particles' signal, therefore the dynamic range of an ADC can not cover the higher harmonics as well. (b) Using a band-stop-filter suppresses both the Drive Field and the particles' signal, moving the dynamic range to the region of the higher harmonics. The first harmonic, however, is lost. (Taken from [5]) . . . . .	7
Figure 6	(a) Concept drawings of the MPI scanner used by Gleich and Weizenecker in 2005 Left: The recording area Right: The field-generating components (b) First acquired MPI image by Gleich and Weizenecker in 2005. (Taken from [1]) . . . . .	8
Figure 7	Overlay of in vivo MPI and MRI images of a mouse at different points in time (axis on the right). Taken from [7]. . . . .	9
Figure 8	MPI-MRI hybrid scanner built by J. Franke et al. (Taken from [8]) . . . . .	10
Figure 9	Concept of Inductive Decoupling: Superimposing the voltage signals (graphs) of two identical coils with opposite winding directions (squares) yields a vanishing output voltage. . . . .	11
Figure 10	The MPI scanner used in the experiments. . . . .	12

Figure 11	(a) A CAD of the coil mounting device used to carry out the experiments. The "mushrooms" ensure fixed coil positions and areas. (b) RC and CC winded on the coil device. Notice that both $L_C$ belong to the CC and are winded with the same wire. The arrows indicate the winding direction. The three marked coils are rectangular and have a span of $170^\circ$ across the coil mounting device. . . . .	13
Figure 12	The MatLab simulation calculates $L_{ik}$ between the DF coil and the RC/CC for different positions of the RC. . . . .	15
Figure 13	(a) Results of the simulation of displacement. $L_{C,DF}$ is the coupling coefficient between the CC and the DF coil, $L_{R,DF}$ the coefficient between the RC and the DF coil. (b) The rate of change of the coupling coefficients $L_{C,DF}$ and $L_{R,DF}$ with the displacement along the x-axis. A higher rate of change means a more error prone measurement. . . . .	16
Figure 14	The MatLab simulation calculates $L_{ik}$ between the DF coil and the RC/CC for different areas of the latter. The simulation is also performed for a displacement of 2.85 cm (not displayed here). . . . .	17
Figure 15	Results of the simulation of distortion. Shown is the coupling coefficient $L_{i,DF}$ between a coil and the DF for different areas of the former, once for alignment along the axis of symmetry of the DF coil, and once for a displacement of 2.58 cm (dashed). . . . .	18
Figure 16	The MatLab simulation calculates $L_{ik}$ between the DF coil and the RC (blue) and the CC (red,dotted). . . . .	19
Figure 17	Equivalent circuit diagram of a real inductivity $L$ . The pictured components are ideal. [5] . . . . .	19
Figure 18	Circuit diagram for Inductive Decoupling . . . . .	20
Figure 19	(a) An LTSpice simulation using ideal components yields $U_C$ (dashed) and $U_R$ with the desired $180^\circ$ phase shift. (b )The same simulation using real components yields an undesired, parasitic phase shift (shown in the enhanced part) between $U_C$ (dashed) and $U_R$ . . . . .	21
Figure 20	Equivalent circuit for real inductor . . . . .	23
Figure 21	Thévenin model of noisy resistor . . . . .	23
Figure 22	Dependency of the SNR on $N$ with $a = 1$ . . . . .	25
Figure 23	The voltages induced by the Drive Field in the Receive Coil $U_R$ and and the Cancellation Coil $U_C$ for (a) the coil mounting device approximately 2 cm displaced from the centre of the gantry, (b) the displacement reduced by 1 cm and (c) the coil mounting device in the middle of the gantry. Depending on the position, either $U_R$ or $U_C$ has a bigger amplitude, therefore, at a certain position (approximately met in (b) ), full compensation is theroretically achievable. Notice that no probe is inserted into the scanner, the signal is solely generated by the Drive Field. . . . .	28

Figure 24	Compensated signal of the Drive Field. A reduction of 55.61 dB has been achieved. . . . .	29
Figure 25	Phase difference $\Delta\varphi$ between two signals and the resulting maximal compensation. . . . .	30
Figure 26	Quadratic fit of $y = p_0 + p_1x + p_2x^2$ to first maximum of $U_R$ measurement in order to determine the frequency of the Drive Field signal. The residuals show a systematic due to the limited voltage resolution of the oscilloscope. . . . .	30
Figure 27	Linear regression of $y = p_0 + p_1x$ to first zero crossing of $U_R$ measurement in order to determine the phase shift to $U_C$ in Fig. 30a. . . . .	31
Figure 28	Circuit diagram of the allpass-filter . . . . .	32
Figure 29	LTS spice simulation showing the effect of an allpass-filter. $U_R$ is the simulated voltage in the Receive Coil. The densely dashed line is the voltage $U_C$ in the Cancellation Coil, phase shifted by $7.3^\circ$ . By increasing the capacitance of $C$ the phase shift is corrected until it is in phase (loosely dashed line). Increasing the capacitance further results in overcompensation (dashed line). . . . .	32
Figure 30	The voltages induced by the Drive Field in the Receive Coil $U_R$ and the Cancellation Coil $U_C$ (a) without an allpass-filter, (b) with an allpass-filter ( $C = (11.24 \pm 0.02)$ pF) attached to the Cancellation Coil, (c) with an allpass-filter attached to the Cancellation Coil and a varied capacitance ( $C = (120.84 \pm 0.24)$ pF) in comparison to (b). . . . .	34
Figure 31	Drive Field induced voltages in the Receive and the Cancellation Coil. The parasitic phase shift is $\Delta\varphi = (7.73 \pm 0.002)$ . . . . .	35
Figure 32	The compensated signal of the voltages shown in Fig. 30 for three different capacitance values of the allpass-filter. By varying the phase shift between the voltages in the Receive and the Cancellation Coil different degrees of compensation are achieved. . . . .	36
Figure 33	The maximum degree of compensation achieved by use of an allpass-filter. Extrinsic noise voltage is clearly visible in this order of magnitude. A reduction of about 66.47 dB has been achieved. . . . .	36
Figure 34	Circuit diagram of the lattice phase equaliser . . . . .	37

## LIST OF TABLES

---

Table 1	MPI in comparison to other modern imaging techniques. (Taken from [2]) . . . . .	5
Table 2	Characterisation of DF coils . . . . .	13
Table 3	Characterisation of RC and CC. Displacement refers to the distance between the centre of the coil and the axis of symmetry of the DF coil. . . . .	14
Table 4	Characterisation of coils . . . . .	20
Table 5	Measured component values of the allpass-filter used in the following experiments. . . . .	33



## MAGNETIC PARTICLE IMAGING

*Magnetic particle imaging* (MPI) is a novel medical imaging technique developed at Philips Research in Hamburg in 2001. After outlining the general concept, the aspect of parasitic coupling effects in MPI is further emphasized in order to point out the field of application of this thesis. Finally, a state-of-the-art report gives a comprehensive view on the widespread research activities in the MPI community.

### 1.1 PRINCIPLE

The concept of MPI was first introduced by Bernhard Gleich and Jürgen Weizenecker in 2005 [1]. The basic principle of this imaging technique is detecting the spatial distribution of *magnetic nanoparticles* (MNP) through their response to a magnetic field. By measuring the voltage induced by the MNP at several points in space, one is able to reconstruct the particle distribution inside a probe and outline it in an image. The application possibilities for MPI are widespread in the medical field, for example diagnosing cardiovascular diseases; however, they are certainly not limited to medical applications.

In order to detect the particle response at a certain point in space, it is necessary to superimpose two<sup>1</sup> magnetic fields:

- The *Drive Field* (DF) is homogeneous in space but sinusoidal in time. It is generated by one pair of Helmholtz coils carrying an alternating current for each spatial dimension.
- The *Selection Field* (SF) is an inhomogeneous field with a constant gradient created by two permanent magnets facing each other with the same pole.

This set-up generates a *field free point* (FFP) in space, where the overall magnetic field strength  $\mathbf{H}$  is zero (Fig. 1).

<sup>1</sup> Some scanners use additional magnetic fields like the *Focus Field* to increase the spatial or temporal resolution of an MPI scanner. The basic functionality, however, is given by the two fields described here.

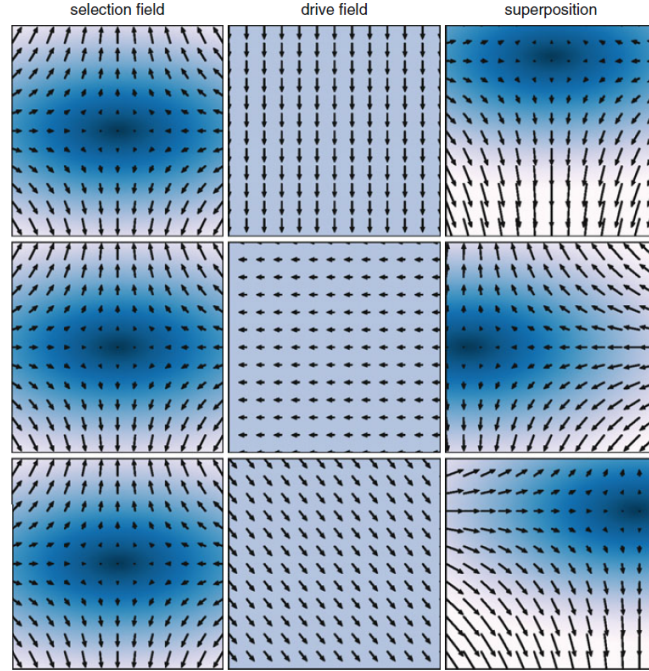


Figure 1: The field lines of the Selection Field, the Drive Field and their superposition for three different phases of the Drive Field to show how the Field Free Point is moved through space. (Taken from [2])

Placing a magnetic particle inside this field will cause it to align its magnetic moment  $\mathbf{m}$  parallel to the external field lines in order to minimise its potential energy. Using the Langevin function

$$L(x) = \coth(x) - \frac{1}{x} \quad (1)$$

one can model the amplitude of the overall magnetisation  $\mathbf{M}$  of a probe containing MNP with

$$M(H) = cm \cdot L(\beta H) \quad (2)$$

using  $\beta = \frac{\mu_0 m}{k_B T^p}$ , i.e. the ratio of magnetic to thermal energy in the system [2]. Here,  $\mu_0$  denotes the vacuum permeability,  $m$  the amplitude of the magnetic moment of a single particle,  $T^p$  the particle temperature and  $k_B$  the Boltzmann constant.  $c$  is the particle concentration in the regarded volume.

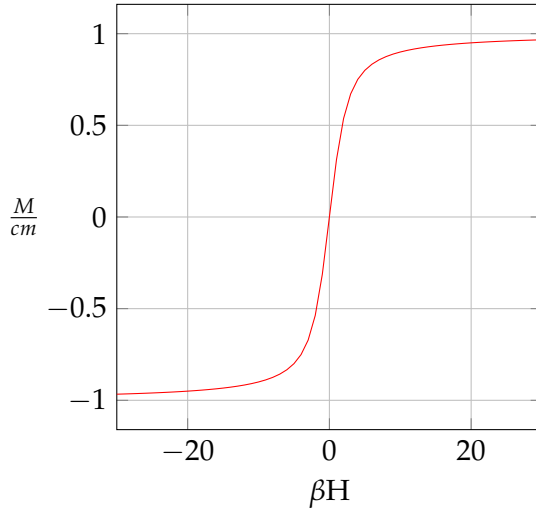


Figure 2: Magnetisation behaviour of magnetic nanoparticles as modelled by the Langevin theory.

Fig. 2 shows that for a small external field strength  $\mathbf{H}$  the probe magnetization  $\mathbf{M}$  undergoes a rapid change in amplitude with a change in  $\mathbf{H}$ , whereas for larger values of  $\mathbf{H}$  saturation effects occur. Therefore, the presented magnetic field enables to get a space-resolved image of the MNP distribution: while the particles outside the FFP are saturated by the selection field, the particles inside it are realigned by the dynamic drive field, and thereby cause a local excitation of the magnetic field at that point.

In order to create a visual representation of the particle distribution, it does not suffice to solely know where the particles are, their concentration  $c$  at that point is required as well. The following calculations shall show that this information is given by the voltage induced by the change of the MNP's magnetic moments  $\mathbf{M}$ .

The external field aligns the magnetic moments of the particles in the FFP. This change in the overall particle magnetization  $\mathbf{M}$  is equivalent to a change in the magnetic flux density  $\mathbf{B} = \mu_0(\mathbf{H} + \mathbf{M})$  and therefore induces an electric field  $\mathbf{E}$  in a plane perpendicular to the direction of the field according to Faraday's law of induction [3]:

$$\nabla \times \mathbf{E} = -\frac{\partial \mathbf{B}}{\partial t} \quad (3)$$

Regarding a single-wire coil, the voltage  $u$  between the two end points can be calculated by integrating the electrical field  $\mathbf{E}$  inside the coil along the conductor:

$$u(t) = \int_{\partial S} \mathbf{E}(\mathbf{l}, t) \cdot d\mathbf{l} \quad (4)$$

Applying Faraday's law and Stoke's theorem to (4) yields

$$\begin{aligned} u(t) &= -\frac{d}{dt} \int_S \mathbf{B} \cdot d\mathbf{A} \\ &= -\mu_0 \left[ \underbrace{\frac{\partial}{\partial t} \int_S \mathbf{H} \cdot d\mathbf{A}}_{\text{Feedthrough Interference}} + \underbrace{\frac{\partial}{\partial t} \int_S \mathbf{M} \cdot d\mathbf{A}}_{\text{Particle Signal}} \right]. \end{aligned} \quad (5)$$

Therefore, a change in  $\mathbf{B}$  due to the alignment of the particles' magnetic momentum  $\mathbf{M}$  leads to a voltage inside the so called *Receive Coil* (RC).

By varying the Selection and Drive Field components of the external field  $\mathbf{H}$ , one can locally induce voltages inside an object containing magnetic nanoparticles and measure their signal with a coil. Repeating this process for the volume of the object to be imaged gives enough information to create a visual representation of it. A simplified set-up is shown in Fig. 3

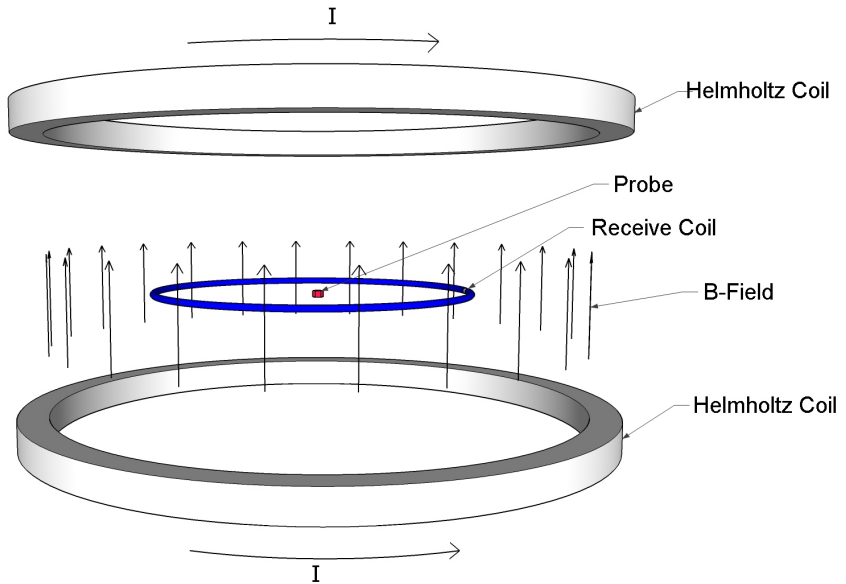


Figure 3: Helmholtz coil pair generates the Drive Field (grey) and the Selection Field (not pictured) by superimposing an alternating current with a direct current. The Receive Coil (blue) picks up the signal of the magnetic nanoparticles (red).

Finally, one question that arises when a new modality is introduced shall be regarded: In which features can it supersede other existing techniques so that further research is reasonable? The following table compares different medical imaging modalities:

	CT	MRI	PET	SPECT	MPI
Spatial resolution	0.5 mm	1 mm	4 mm	10 mm	<1mm
Acquisition time	1 s	1 s-1 h	1 min	1 min	<0.1 s
Sensitivity	Low	Low	High	High	High
Quantifiability	Yes	No	Yes	Yes	Yes
Harmfulness	X-ray	Heating	$\beta/\gamma$ radiation	$\gamma$ radiation	Heating

Table 1: MPI in comparison to other modern imaging techniques. (Taken from [2])

Tab. 1 shows that the strength of MPI is a high temporal and spatial resolution without the emission of harmful radiation. A special charm is given by the similarity to *magnetic resonance imaging* (MRI) in hardware aspects. Both concepts utilise magnetic fields and administer *superparamagnetic iron oxide nanoparticles* (SPIONs) to the patient. Since MRI measures the local response of the tissue, it takes tomographic images of the morphology, while MPI measures the tracer material itself, revealing functional aspects, e.g. the blood flow. A combination of these imaging modalities promises an exciting look inside the body [4].

## 1.2 COUPLING PROBLEM

The set-up described above has an inherent problem, as shown in Eq. 5. The voltage in the RC is a superposition of the signal induced by the change in magnetic momentum  $\mathbf{M}$  of the particles and, in addition, of the signal induced by the change in external field strength  $\mathbf{H}$ , i.e. the DF that is used to excite the particles. A closer look at both signals shows that this limits the resolution of MPI.

Due to the non-linear magnetisation response of the MNP (Fig. 2), the induced particle signal is not sinusoidal as the DF signal (Fig. 4, top), but distorted into a voltage peak. While in time domain, the particles' signal is indistinguishable from the DF signal due to its amplitude, which is about six orders-of-magnitude lower than the one of the DF signal, in frequency domain, it is characterised by higher harmonics of the fundamental frequency  $f_0$ , i.e. the DF frequency (Fig. 4, middle). This is shown in [2] by expanding the Langevin function into a Taylor series for  $x \ll 1$ :

$$L(x) = \frac{1}{3}x - \frac{1}{45}x^3 + \frac{2}{954}x^5 - \frac{1}{4.725}x^7 + \dots \quad (6)$$

The series shows that for a sinusoidal excitation, all odd higher harmonics are non zero (see Eq. 2).

The first harmonic of the resulting signal in the RC is a superposition of the DF and the particles' signal, with the latter being six orders of magnitude lower than the former (Fig. 4, bottom) [5].

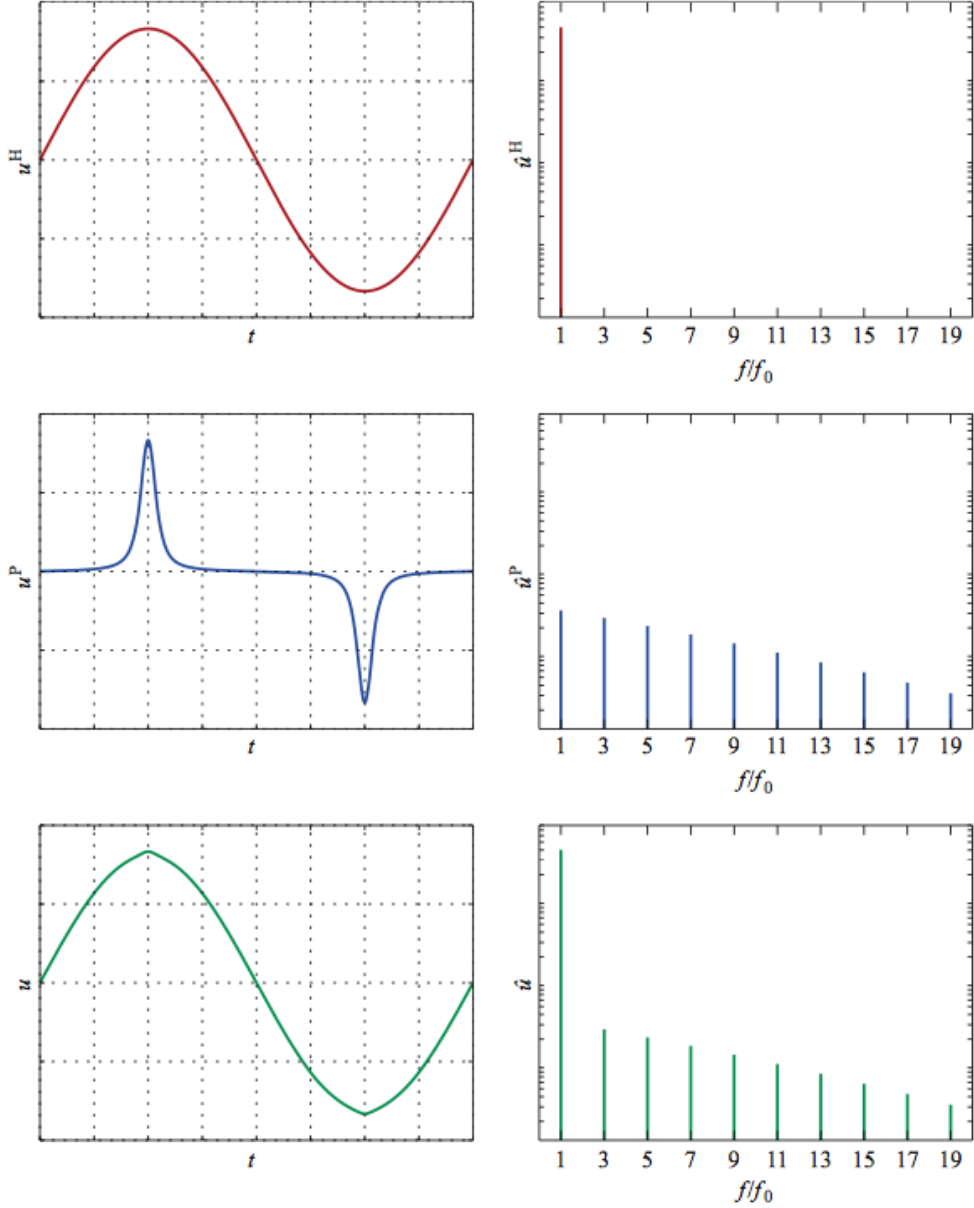


Figure 4: The induced voltages in the Receive Coil and the amplitudes of their Fourier coefficients. The Drive Field signal (Top) is sinusoidal, while the particles' signal (Middle) resembles spikes due to the non-linearity of the magnetisation behaviour. The Fourier coefficient of the fundamental frequency  $f_0$  of the resulting signal (Bottom) is a superposition of the Drive Field and the particles' signal, the higher harmonics solely result from the particles' signal. (Taken from [2])

Since MPI relies on the particles' signal to determine the concentration of the MNP inside the probe volume, it is evident that one wants to differentiate between the fraction of the first harmonic caused by the DF and the one belonging to the particles'

signal, as the first harmonic carries the most information about the voltage. However, due to the large difference in amplitude and the finite dynamic range of an *analog-to-digital converter* (ADC), it is not possible to do that digitally. Fig. 5 illustrates the problem. Most MPI scanners use band-stop-filters to attenuate the first harmonic and thereby move the dynamic range into the region of the higher harmonics; however, this also suppresses part of the particles' signal.

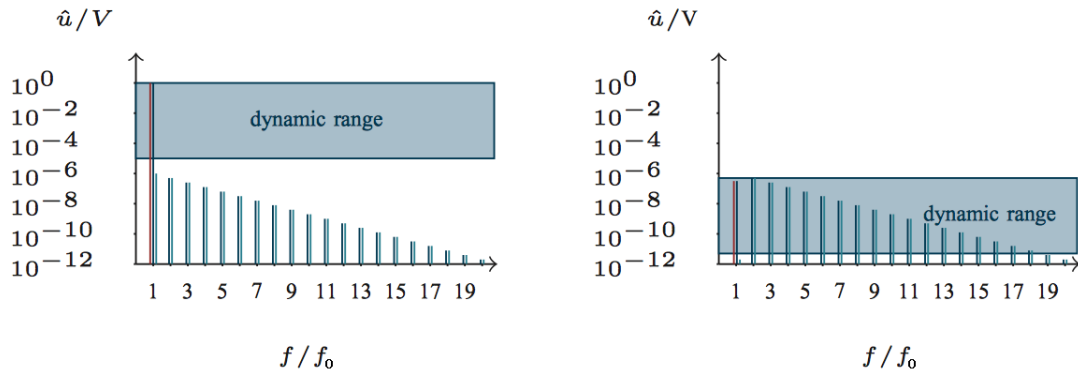


Figure 5: (a) The overall signal (left) is the superimposed feedthrough interference of the Drive Field signal (middle) and the particles' signal (right). The interference is several orders of magnitude higher than particles' signal, therefore the dynamic range of an ADC can not cover the higher harmonics as well. (b) Using a band-stop-filter suppresses both the Drive Field and the particles' signal, moving the dynamic range to the region of the higher harmonics. The first harmonic, however, is lost. (Taken from [5])

An alternative to using a filter is the application of a second coil, identical to the RC, which only picks up the DF signal. This concept, known from MRI, was introduced to MPI by Graeser et al. [5] in 2013 and further examined by Schulz et al. [6] in 2014. This thesis follows up on the work presented in [6].

### 1.3 STATE OF THE ART

In 2005, Bernhard Gleich and Jürgen Weizenecker first published a journal article in *Nature* presenting the idea of MPI and showing its feasibility with images of a 2D phantom probe [1]. Fig. 6a shows the coil arrangement, which is identical to the one shown in Fig. 3, while Fig. 6b shows the acquired image of the P-shaped phantom.

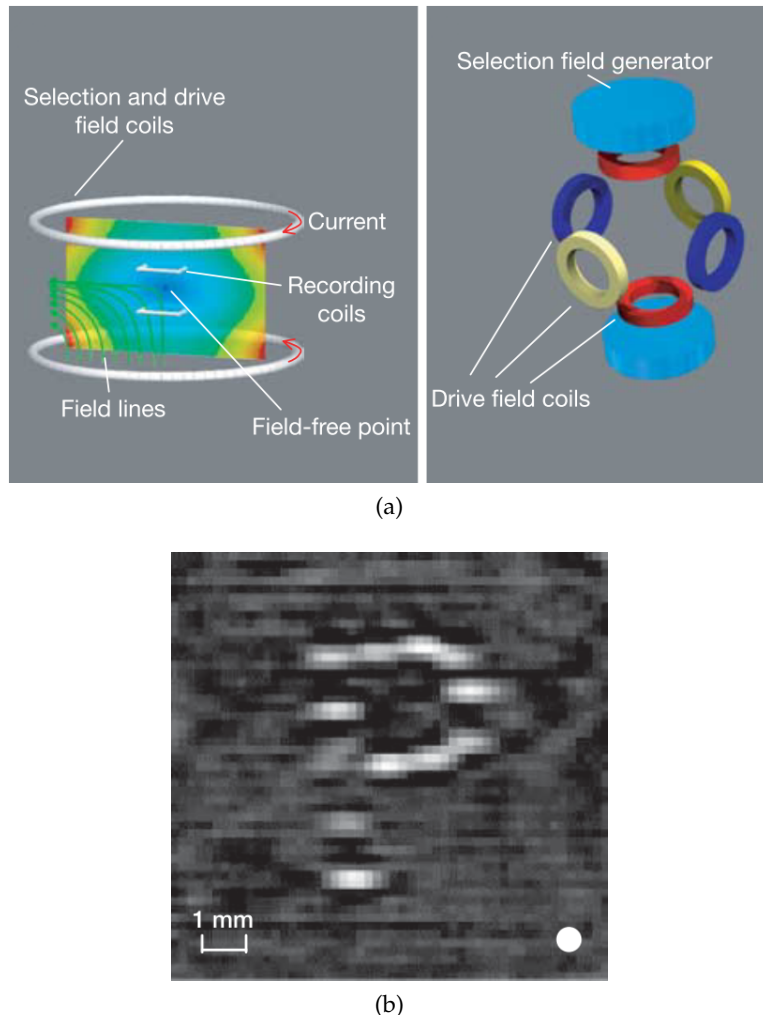


Figure 6: (a) Concept drawings of the MPI scanner used by Gleich and Weizenecker in 2005

Left: The recording area

Right: The field-generating components

(b) First acquired MPI image by Gleich and Weizenecker in 2005. (Taken from [1])

The next milestone was taken in 2009, when Weizenecker et al. published their results of a "three-dimensional real time *in vivo* magnetic particle imaging" [7]. They successfully imaged the tracer material inside a beating mouse heart with a temporal resolution of 21.5 ms and a spatial one sufficient to distinguish single heart chambers. By overlaying the MPI measurements with images taken by *magnetic resonance imaging* (MRI), details of the blood flow in the mouse were revealed (Fig. 7).

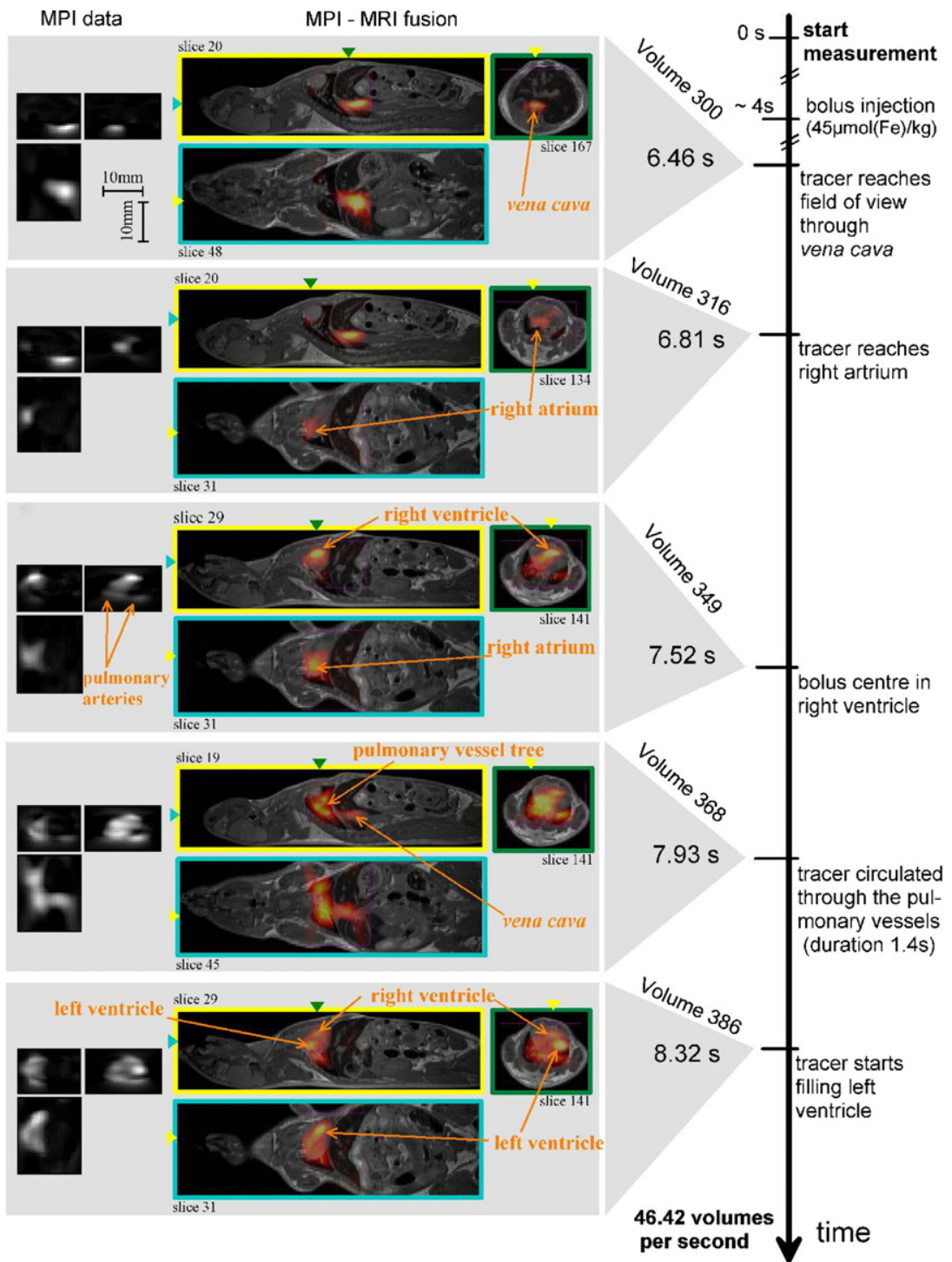


Figure 7: Overlay of in vivo MPI and MRI images of a mouse at different points in time (axis on the right). Taken from [7].

While Weizenecker et al. used two standalone set-ups for MPI and MRI images, the first hybrid MPI-MRI scanner (Fig. 8) is also being built by J. Franke et al. at Bruker BioSpin MRI GmbH [8]. They arranged the needed magnetic components

concentrically and are able to sequentially take both MPI and MRI images without moving the probe.



Figure 8: MPI-MRI hybrid scanner built by J. Franke et al. (Taken from [8])

The coupling problem described in [Section 1.2](#) is being investigated in Lübeck by M. Graeser et al., who proposed in [5] a combination of filtering the fundamental frequency and using a cancellation signal chain in order to preserve the first harmonic of the particles' signal. Besides using a second receive coil to cancel out feedthrough interference, they also investigated using a second, identical send and receive chain as a reference system. However, due to the high power consumption of such a set-up, duplicating the scanner seemed not feasible to them. Using the second coil for cancellation, they were able to improve the SNR and image quality of the scanner. In addition, the MPI research community is exploring new ways to optimise the imaging modality, for example by utilising new DF coil topologies to achieve a so called *Travelling-Wave-MPI* [9] or by expanding the FFP to a field free line in order to increase sensitivity [10].

# 2

## INDUCTIVE DECOUPLING

This chapter examines the *Inductive Decoupling* method of decoupling the Drive Field and the Receive Coil. First, the principle is outlined. Simulation studies then aim to determine possible error sources and propose the optimal parameters of the coils.

### 2.1 PRINCIPLE

The following concept of inductive decoupling originates in the *Neumann Formula* for the mutual inductance coefficient  $L_{kl}$  of two coupled inductors [11].

$$L_{kl} = \frac{\mu_0}{4\pi} \int_{C_k} \int_{C_l} \frac{d\mathbf{r} \cdot d\mathbf{s}}{|\mathbf{r} - \mathbf{s}|} \quad (7)$$

$C_k$  and  $C_l$  represent the paths over the conductor loops,  $d\mathbf{r}$  and  $d\mathbf{s}$  are differential path elements.

The definition of a definite integral states that reversing the path integral over  $C_l$  results in the same coefficient, however, with a changed sign:

$$L_{kl} = -L_{k,-l}$$

Reversing the path of integration is electronically achieved by reversing the winding direction of the inductor.

To apply this formula to the coupling problem described in [Section 1.2](#), an additional coil is introduced, the *Compensation Coil* (CC). If the Receive and the Compensation Coil are identical in their properties and layout but differ in their winding directions, the superposition of both induced voltage signals should be equal to zero ([Fig. 9](#)).

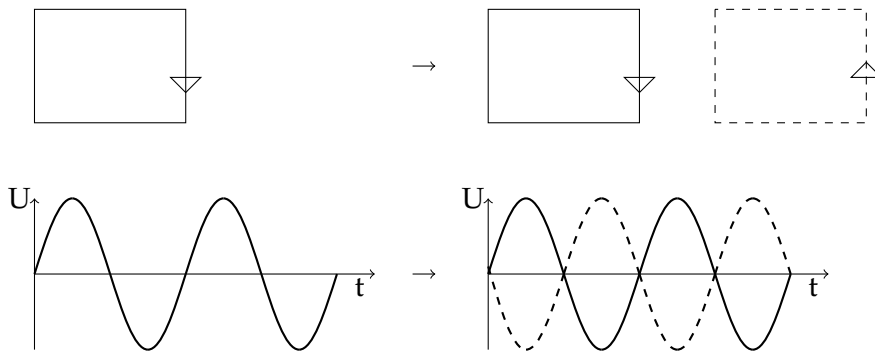


Figure 9: Concept of Inductive Decoupling: Superimposing the voltage signals (graphs) of two identical coils with opposite winding directions (squares) yields a vanishing output voltage.

[Fig. 18](#) shows the resulting circuit diagram. To minimise the probe signal pick up, the actual set-up uses two CCs, one on either side of the RC (see [Fig. 11b](#)).

## 2.2 THE SCANNER

The MPI scanner that is used to carry out the experiments is the first MPI scanner built by Bernhard Gleich and Jürgen Weizenecker (Fig. 10) and the one that was used in their *in vivo* magnetic particle imaging described in [Section 1.3](#). While it was built at Philips Research in Hamburg, it is currently on permanent loan to the RWTH Aachen University.

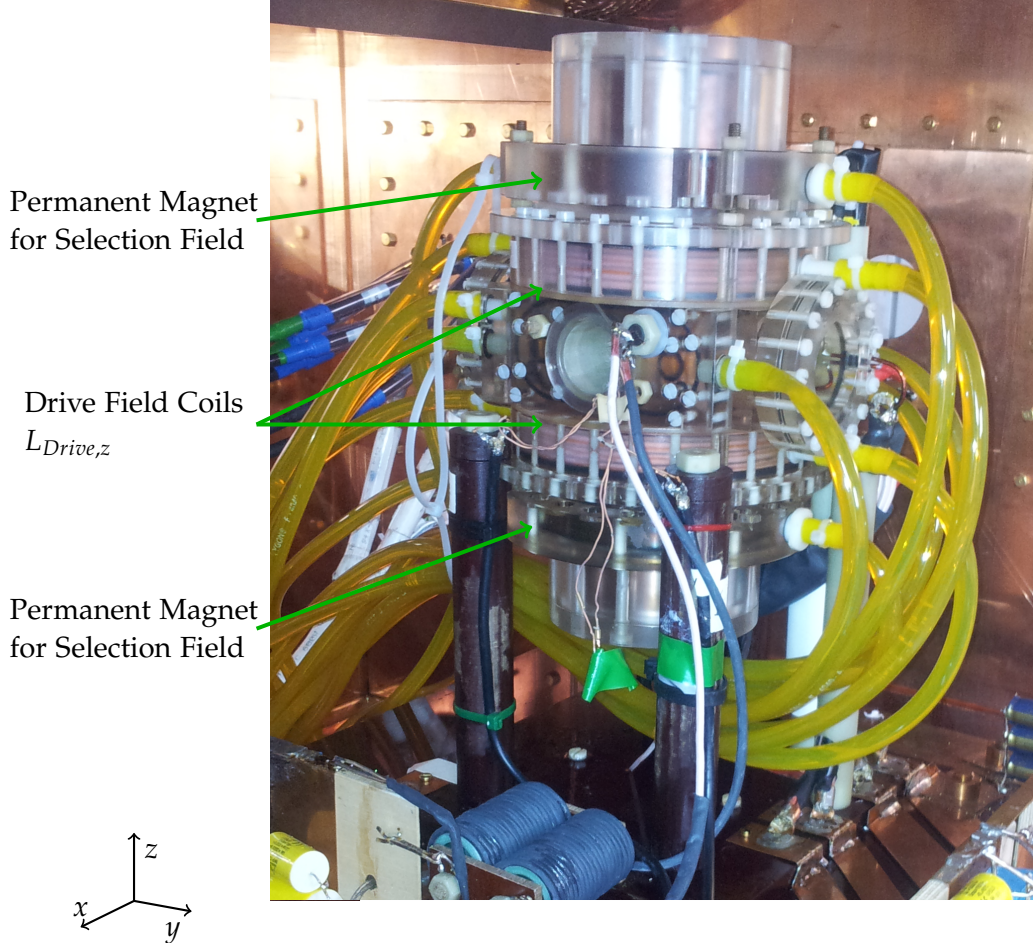


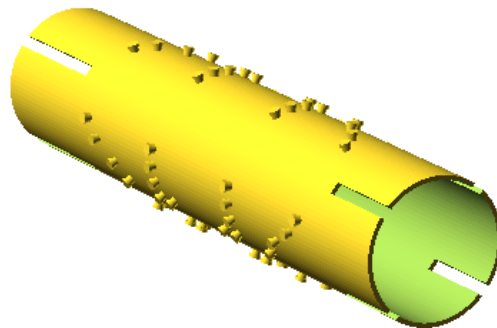
Figure 10: The MPI scanner used in the experiments.

The scanner uses permanent magnets for generating the Selection Field and Helmholtz coil pairs for the DF. It is embedded in a copper box to minimise external influences. The DF coils have the following properties (Tab. 2), where the second index states the axis of symmetry of the Helmholtz coil pair.

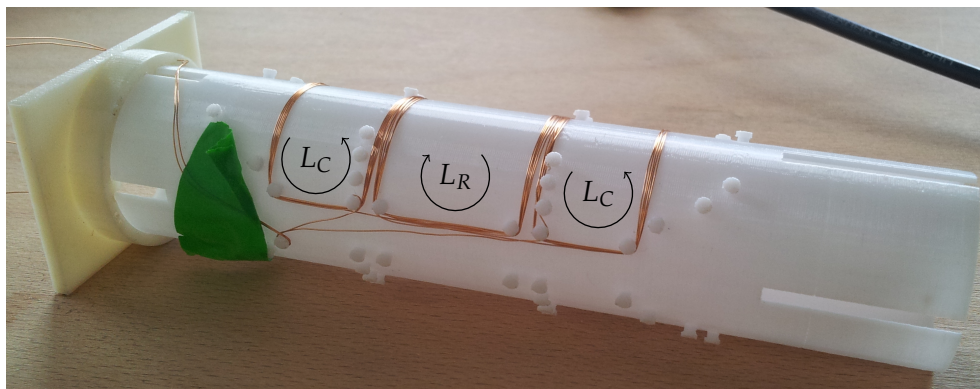
DRIVE FIELD COIL	$L / \mu\text{H}$	$Z / \Omega$
$\mathbf{L}_{Drive,x}$	116.4	0.7
$\mathbf{L}_{Drive,y}$	24	0.02
$\mathbf{L}_{Drive,z}$	167	0.2

Table 2: Characterisation of DF coils

The coil mounting device is a 3D printed plastic tube, which allows for coils to be wound so that the coupling coefficients  $L_{ik}$  are theoretically equal (Fig. 11a). It is the same device which was used in Schulz et al. paper [6]. Fig. 11b shows the actual coil mounting device with the coils wended onto it.



(a)



(b)

Figure 11: (a) A CAD of the coil mounting device used to carry out the experiments. The "mushrooms" ensure fixed coil positions and areas. (b) RC and CC wended on the coil device. Notice that both  $L_C$  belong to the CC and are wended with the same wire. The arrows indicate the winding direction. The three marked coils are rectangular and have a span of 170° across the coil mounting device.

## 2.3 SIMULATIONS

While Inductive Decoupling in principle is a simple concept, it has potential sources of errors. The following simulation studies aim to determine these and estimate their impact.

### 2.3.1 Displacement and Distortion Effects

One condition for Inductive Decoupling to work is the exact alignment and adjustment of the Receive and the Compensation Coils to each other, in order to achieve the same coupling amplitude between the drive field and the coils. Therefore, it is reasonable to simulate  $L_{ik}$  for small deviations in position and size and estimate the effects of displacement and malformation.

The coupling coefficient between the Drive Field coil and a single, rectangular coil representing either Receive or Compensation Coil is calculated numerically using the *MatLab* software (*The MathWorks, Natick, MA, US*) and Equ. 7. A rectangle is a good estimate for the actual shape of the coils used in the later measurements (see Fig. 11b).

First, the position of the rectangular coil is varied stepwise, from the centre of the rectangle<sup>1</sup> being directly underneath the centre of the drive field coil, to a displacement of 6 cm along the x-axis (Fig. 12).

As the existing DF coil is embedded inside the scanner, its radius is only estimated, however, due to the investigative nature of the simulation, the correct order of magnitude is sufficient. The properties of the Receive and the Cancellation Coil are extracted from the CAD drawing of the coil device (Tab. 3). The Receive Coil is at the centre of symmetry of the DF coil, while the two rectangular parts of the CC are displaced by 2.85 cm (see Fig. 12).

COIL	WIDTH / CM	LENGTH / CM	DISPLACEMENT / CM
RC	3.5	2.7	0
CC	3.5	2.2	2.85

Table 3: Characterisation of RC and CC. Displacement refers to the distance between the centre of the coil and the axis of symmetry of the DF coil.

<sup>1</sup> Here, the centre of a rectangle is the point of intersection of the perpendicular bisectors of the sides

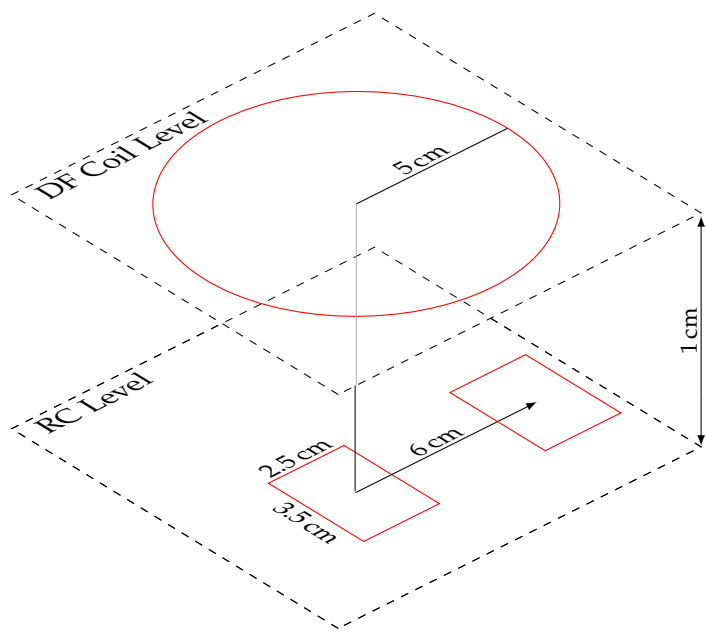


Figure 12: The MatLab simulation calculates  $L_{ik}$  between the DF coil and the RC/CC for different positions of the RC.

The simulation is performed twice, once with the parameters of the RC and once with the ones of the CC. The results are shown in Fig. 13a.

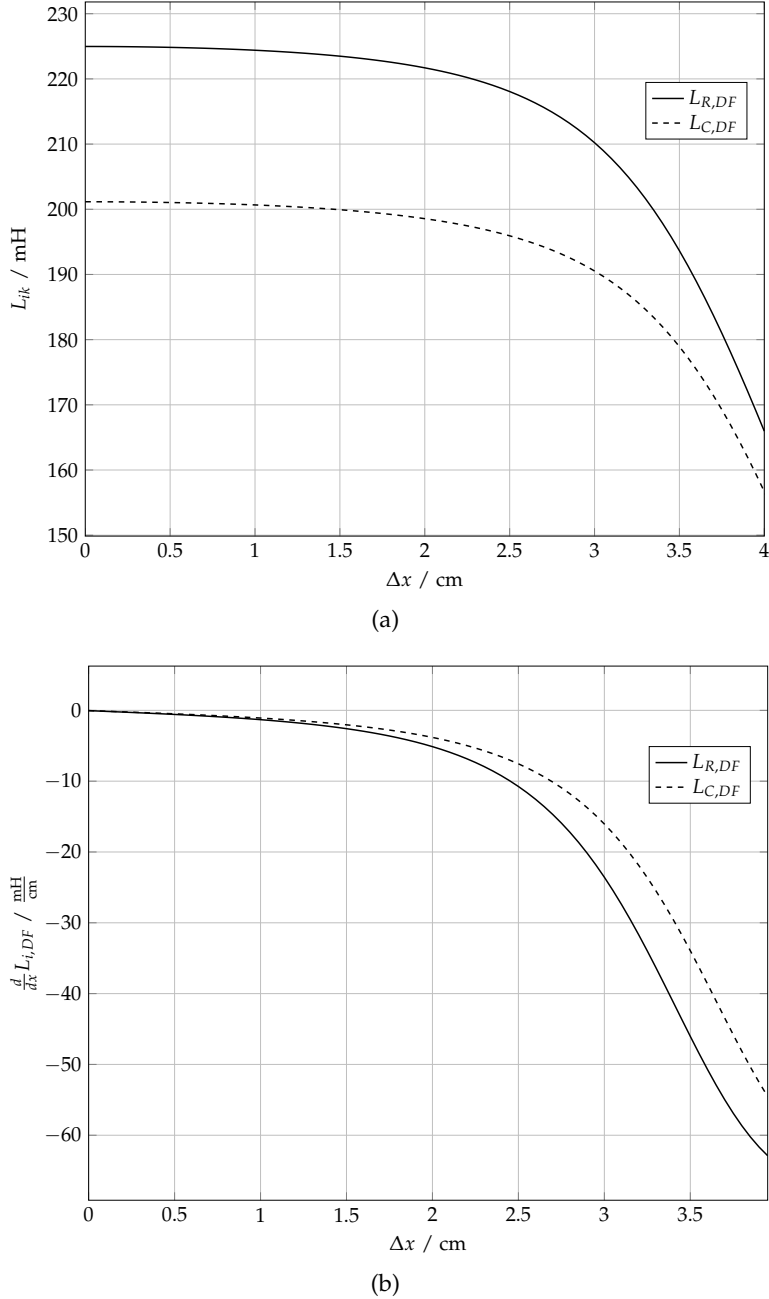


Figure 13: (a) Results of the simulation of displacement.  $L_{C,DF}$  is the coupling coefficient between the CC and the DF coil,  $L_{R,DF}$  the coefficient between the RC and the DF coil. (b) The rate of change of the coupling coefficients  $L_{C,DF}$  and  $L_{R,DF}$  with the displacement along the x-axis. A higher rate of change means a more error prone measurement.

The simulation shows that positioning the coils close to the axis of symmetry of the DF coil is preferable over farther away. The coupling coefficients are larger and vary less for smaller displacements, so a small deviation has a negligible effect. The RC therefore is at the right position.

Due to its smaller error and larger displacement, the CC has a lower coupling coefficient and is more prone to positioning errors. The rate of change  $d/dx L_{C,DF}$  is

-12.3 mH/cm, so a displacement of only 1 mm would cause a drop of 0.6 % in the coupling coefficient. In terms of error susceptibility, it would be reasonable to further displace the CC to about 3.25 cm. The linear rate of change here offers an advantage: displacing the coil mounting device by a small distance would increase the coupling coefficient of half of the CC while decreasing the one of the other half by the same amount, yielding a vanishing error.

All in all, this analysis shows that the displacement of coils has to be regarded as an error source for the CC, while in practice it also offers an advantage: Moving the coil mounting device along the probe tunnel is the only method to align the coupling voltages in the RC and CC during the experiment, enabling the compensation of previously unregarded error sources.

Next, a simulation is performed to estimate the impact if the RC and CC have different areas than expected, e.g. if they are winded inaccurately. The coupling coefficient is calculated for coils of different lengths aligned to the centre of symmetry of the DF coil and in addition displaced by 2.85 cm (see Fig. 14).

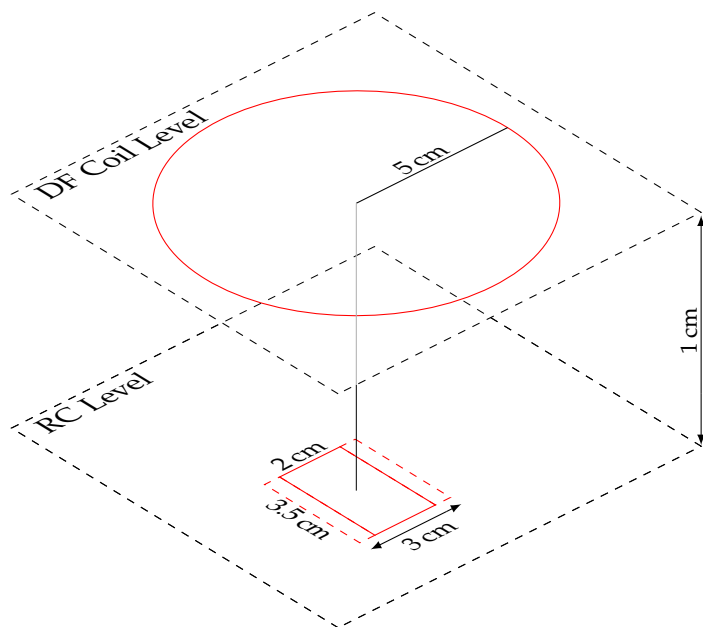


Figure 14: The MatLab simulation calculates  $L_{ik}$  between the DF coil and the RC/CC for different areas of the latter. The simulation is also performed for a displacement of 2.85 cm (not displayed here).

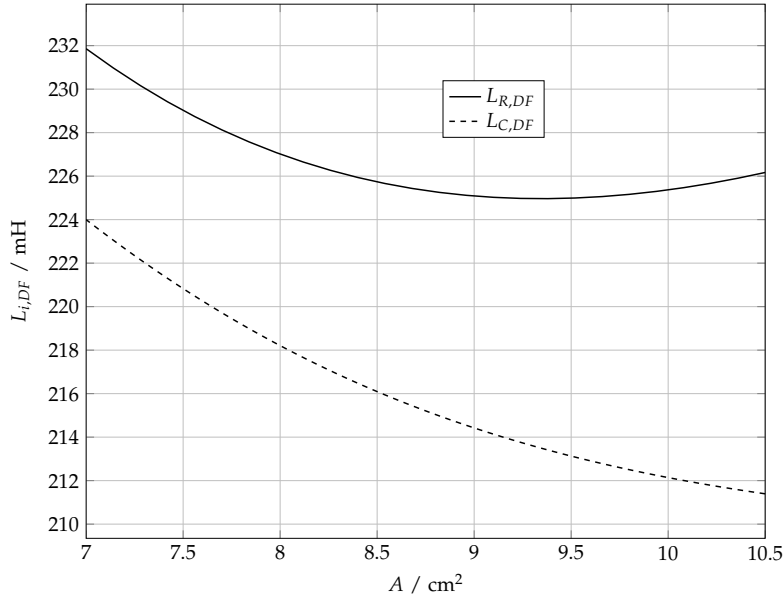


Figure 15: Results of the simulation of distortion. Shown is the coupling coefficient  $L_{i,DF}$  between a coil and the DF for different areas of the former, once for alignment along the axis of symmetry of the DF coil, and once for a displacement of 2.58 cm (dashed).

The relation between  $L_{ik}$  and the RC area  $A$  shows an interesting behaviour as it has a minimum at about  $9.4 \text{ cm}^2$ . Coils with this area are the least susceptible to area deviations. The minimum seems to be an effect of the circle-rectangle-combination in this calculation, a simulation with two circles yielded a constant rate of change as one would expect it for a constant increase in area.

The simulation shows that the CC is more susceptible to area deviations than the RC with an area of  $9.45 \text{ cm}^2$  since the CC is made of two (congruent) rectangular areas with an area of  $7.7 \text{ cm}^2$  each. However, as pointed out above, this error source can be compensated by varying the position of the coil mounting device in the scanner.

Now, a last MatLab simulation is performed to calculate the actual coupling coefficients of the RC and the CC (Fig. 16).

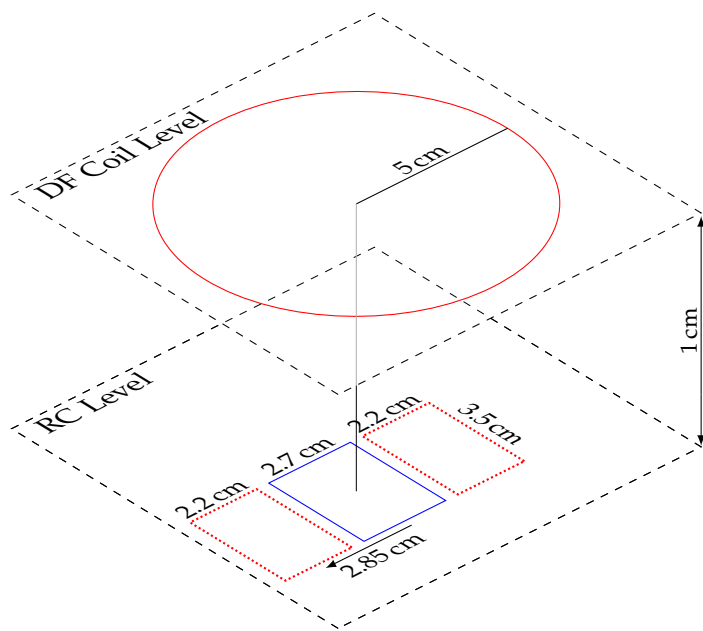


Figure 16: The MatLab simulation calculates  $L_{ik}$  between the DF coil and the RC (blue) and the CC (red,dotted).

The calculation yields  $L_{DF,RC}=225.0\text{ mH}$  and  $L_{DF,CC}=192.6\text{ mH}$ , in accordance with the simulations above.

### 2.3.2 Electrical Effects

Next, the effect of the parasitic quantities of a circuit made of real components is analysed. While an ideal coil component only exhibits inductive behaviour in an electric circuit, the real component adds unwanted capacities and resistances, which exert a direct impact on the voltages inside the circuit. Phase shifts and amplitude losses are common examples. An equivalent circuit diagram is shown in Fig.17.

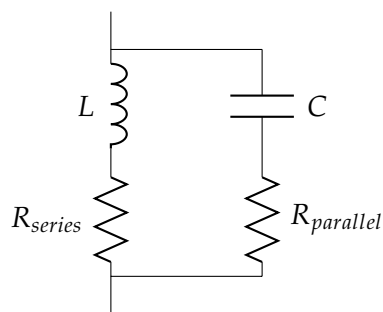


Figure 17: Equivalent circuit diagram of a real inductivity  $L$ . The pictured components are ideal. [5]

In order to estimate the impact, an RC and a CC are wound on a coil device (Fig. 11b). The electronic properties of these coils are then measured with an LCR-meter<sup>2</sup> (see Tab. 4). While every quantity has an error of 0.2% according to the manufacturer [12], it is not listed below as does not contribute to the simulation.

COIL	$L / \mu\text{H}$	$C / \mu\text{F}$	$Z / \Omega$
Receive	4.00	63.23	1.09
Compensation	5.33	47.55	2.17

Table 4: Characterisation of coils

The electric circuit shown in Fig. 18 is then simulated using the *LTS spice* software and the measured attributes of the coils. The values of the z-channel of the drive field are plugged in for the drive field (see Tab. 2).

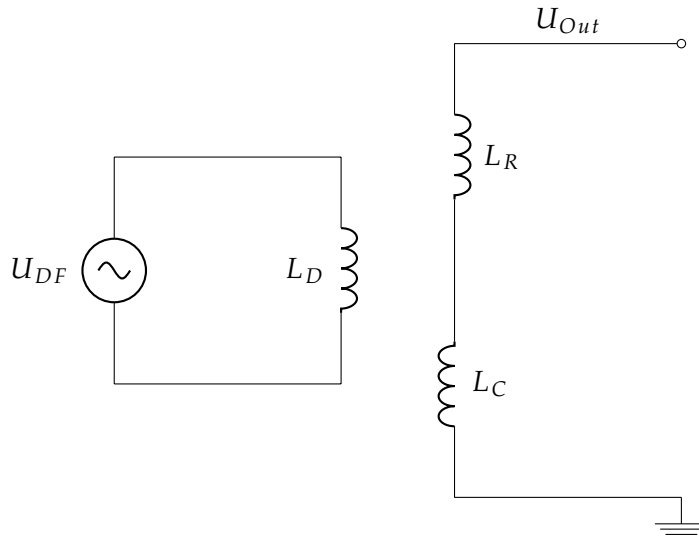


Figure 18: Circuit diagram for Inductive Decoupling

In Fig. 19a, the circuit is simulated using ideal components, Fig. 19b shows the resulting voltages for real components.

<sup>2</sup> Agilent U1733C

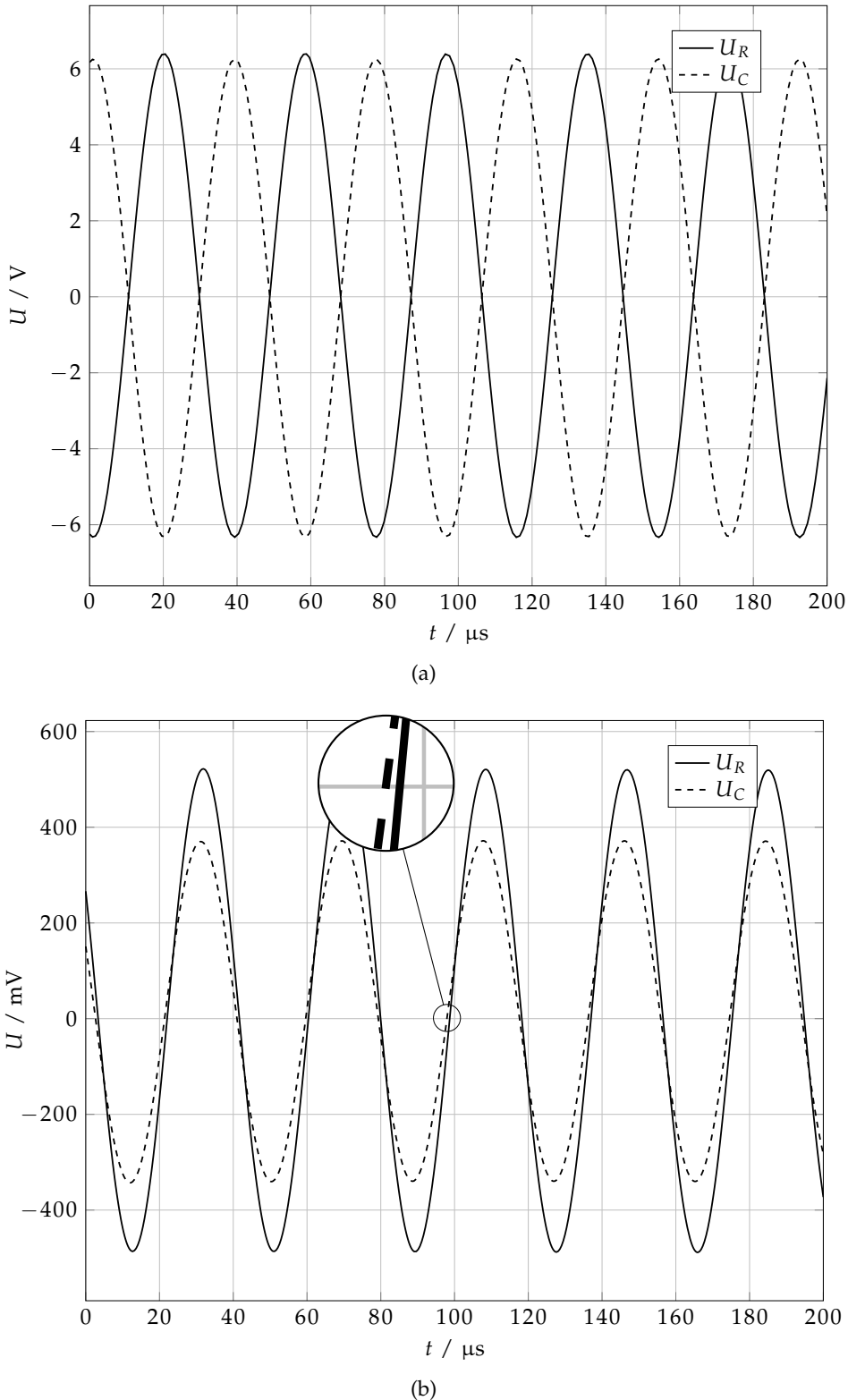


Figure 19: (a) An LTSpice simulation using ideal components yields  $U_C$  (dashed) and  $U_R$  with the desired  $180^\circ$  phase shift. (b) The same simulation using real components yields an undesired, parasitic phase shift (shown in the enhanced part) between  $U_C$  (dashed) and  $U_R$ .

The desired phase shift of  $180^\circ$  between the two voltages is not plotted in Fig. 19b as to differentiate it from the undesired parasitic phase difference  $\Delta\varphi$ . To calculate the latter, the following ratios are compared:

$$\frac{\Delta\varphi}{360^\circ} = \frac{\Delta t}{T} \quad (8)$$

Here,  $T$  is cycle duration of the oscillations and  $\Delta t$  the time difference between two points of the same phase. Using the LTSpice data to determine these values in Fig. 19b, the simulated phase difference due to parasitic quantities equals  $\Delta\varphi = 6.5^\circ$ .

In addition to the phase shift, a change in amplitude is observable as well due to the parasitic resistances.

## 2.4 SIGNAL-TO-NOISE RATIO

The following analysis examines the *signal-to-noise ratio* (SNR) of the Inductive Decoupling method, defined as [13]

$$SNR = 10 \cdot \log(u_s^2 / u_n^2). \quad (9)$$

Here,  $u_s$  is the particle signal and  $u_n$  the interfering electronic noise. The definition shows that a higher SNR is preferable over a lower one as it means low noise interference and high signal amplitude.

The following section will show that the electronic noise is solely dependent on the resistance  $R$  of the complete circuit, while the signal voltage has a variety of defining factors, e.g. the concentration of the particles or the probe volume. As these factors are dependent on the specific measurement and have no immediate effect on the noise, only the factor that influences both quantities will be regarded: the number of coil windings  $N$ . It is reasonable to assume that both  $u_s$  and  $u_n$  increase with  $N$ , however, the following calculations shall give a closer look at the dependencies on  $N$ .

### 2.4.1 Electronic Noise

The measurable quantities of electronic circuits, e.g. voltage and current, are superimposed by noise signals of various sources. These signals present a perturbation and can render a measurement useless, especially if the obtained quantities are of the same magnitude. In general, a differentiation between two types of noise is made [13]:

- **Intrinsic source:** Noise that is caused by the components within the circuit itself.
- **Extrinsic source:** Noise that is caused by electronic components within the vicinity of the circuit.

The latter will not be discussed in this thesis as it is highly dependent on the specific surrounding. It is however the reason why the SNR is only calculated and not measured in this thesis: A complete characterisation of the extrinsic noise inside the

field of view is yet to be performed and thereby a measurement of the intrinsic is rendered useless.

There are several sources of intrinsic noise, most of which find their physical origin in the randomness of quantum particles. For instance, the Brownian motion of the electric charge carriers inside a copper wire causes random displacement of particles which induces a measurable voltage within the wire, the so called *thermal noise*. This is the main source of noise in dissipative systems, e.g. a resistor. The resulting voltage fluctuations are a shift of thermal energy to energy of the electric field.

In 1928, Harry Nyquist published an article in which he derived a description of thermal noise using the second law of thermodynamics [14]. He showed that the noise voltage  $u_n$  is given by

$$u_n = \sqrt{4kT R \Delta f}. \quad (10)$$

Here,  $\Delta f$  is the frequency bandwidth,  $k_B$  the Boltzmann constant,  $T$  the coil temperature and  $R$  the value of the noisy resistance.

Since Eq. 10 is independent of the frequency, thermal noise is so called white noise.

In the following calculations, the inductors are modelled as their equivalent circuits (Fig. 20) with the parasitic resistance as a single resistor. The noisy resistors are then split up into a noiseless resistor and a voltage source, following the Thévenin model [13] of noisy resistors (Fig. 21).

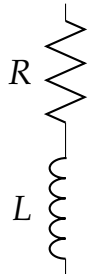


Figure 20: Equivalent circuit for real inductor

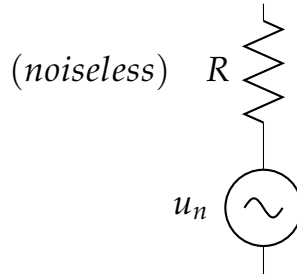


Figure 21: Thévenin model of noisy resistor

#### 2.4.2 Noise Calculation

The voltage fluctuations are statistical variables without a correlation to each other. Therefore, the total noise of the circuit is given by the quadratic addition of the single noise voltages<sup>3</sup>:

$$u_{n, total} = \sqrt{u_{n,L_R}^2 + u_{n,L_C}^2} \quad (11)$$

---

<sup>3</sup> Though the CC does not contribute any signal to the SNR, its noise has to be looked at since it contributes to the circuit noise.

The resistance  $R$  of each coil is given by

$$R = N \cdot \frac{\rho \cdot l_w}{A} \quad (12)$$

with  $\rho$  the specific electrical resistance of copper,  $l_w$  the length of one winding,  $A$  the cross sectional area of the copper wire and  $N$  the number of windings. Therefore, the dependency of the noise voltage  $u_n$  of  $N$  is:

$$u_n \propto \sqrt{N} \quad (13)$$

Plugging the resistance values of Tab. 4 into Equ. 11 yields an overall voltage noise of  $232.41\text{pV}/\sqrt{\text{Hz}}$  at  $300\text{K}$  room temperature.

#### 2.4.3 Probe Signal

As shown in Section 1.1, the probe signal induced in the RC is given by:

$$u^s(t) = -\mu_0 \int_{\text{probe}} \mathbf{p}^{RC}(\mathbf{r}) \cdot \frac{\partial \mathbf{M}(\mathbf{r}, t)}{\partial t} d^3r \quad (14)$$

Here,  $\mathbf{p}^{RC}(\mathbf{r})$  is the RC sensitivity, i.e. the ratio of the magnetic field strength  $\mathbf{H}$  that the RC generates and the current  $I$  flowing through it:  $\mathbf{p}^{RC}(\mathbf{r}) = \mathbf{H}^{RC}/I^{RC}$ . As the magnetic field strength of a conductor loop is proportional to its number of windings  $N$  [3], it follows that the sensitivity  $\mathbf{p}^{RC}(\mathbf{r})$  and therefore the probe signal  $u^s(t)$  are proportional to it as well.

$$u^s(t) \propto N \quad (15)$$

After determining these dependencies, one can adjust Eq. 9:

$$SNR = 10 \cdot \log(u_s^2/\overline{u_n^2}) = a \cdot \log(N) \quad (16)$$

where  $a$  is a scaling factor independent of  $N$ .

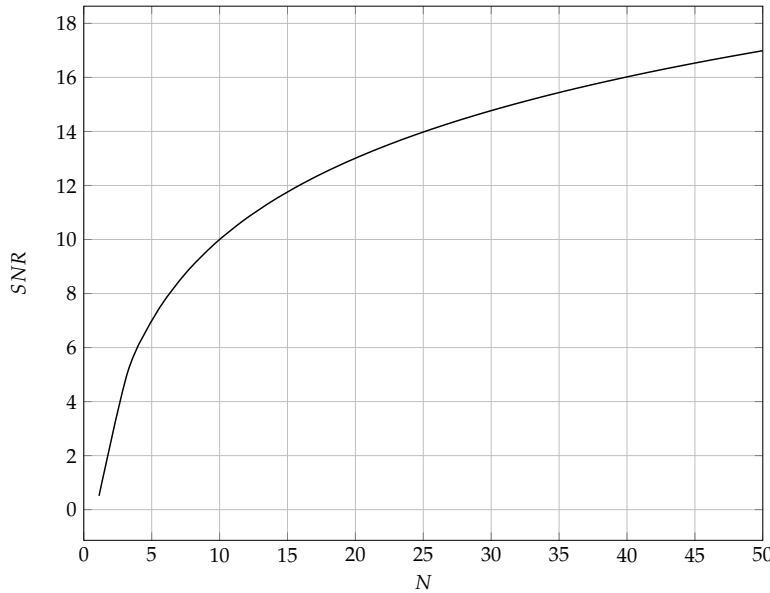


Figure 22: Dependency of the  $SNR$  on  $N$  with  $a = 1$ .

Fig. 22 shows that theoretically an infinite number of windings would be best, however, while it is not only not feasible, one would also get unwanted parasitic effects due to capacitive coupling between the single windings. Overall, increasing  $N$  up to about 10 seems sensible as it results in a big increase of the  $SNR$ .



# 3

## MEASUREMENTS

---

Ensuing to the simulations and calculations in [Chapter 2](#), measurements are performed to try out the Inductive Decoupling method in practice. The noise calculation in [Section 2.4.2](#) showed that even with complete compensation one would obtain a signal in the range of picovolt, simply due to the random movement of the charge carriers. In [Section 1.2](#) it was shown that the cancellation method is sufficient when the dynamic range of the ADC covers the DF signal in addition to the higher harmonics of the particles' signal. Therefore, a compensation of the DF signal by six orders-of-magnitude would mean a successful decoupling of the Drive Field and the Receive Coil. However, this degree of compensation is not a realistic aim in the following experiments, since they are of investigative nature and offer room for improvement. Therefore, the following measurements are to be regarded more as a proof of concept than a representation of the full potential of the Inductive Decoupling method.

### 3.1 FEEDTHROUGH INTERFERENCE MEASUREMENT

After placing the coil mounting device inside the gantry, its position is adjusted until the voltage signals  $U_R$  and  $U_C$  have about the same amplitude ([Fig. 23](#)). It is evident that the voltages are dependent on the position of the coil mounting device and, in addition, differ in their dependency, as [Fig. 23](#) shows.

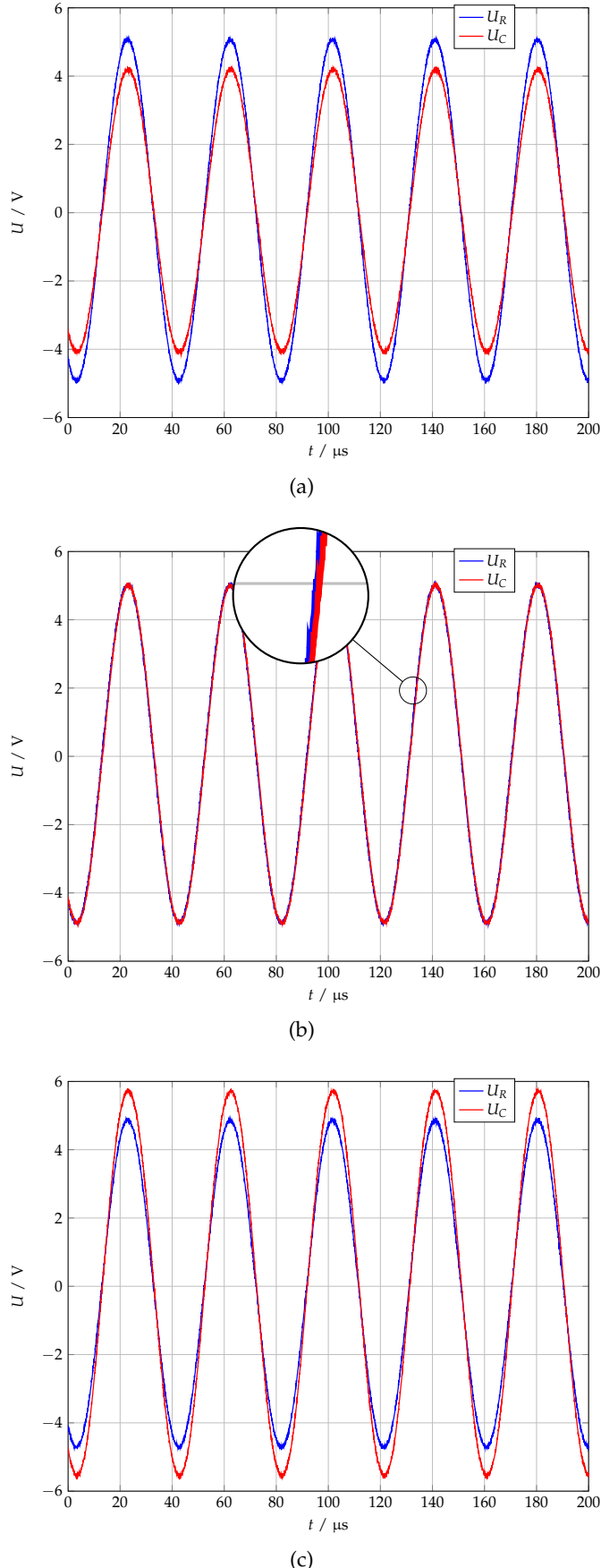


Figure 23: The voltages induced by the Drive Field in the Receive Coil  $U_R$  and the Cancellation Coil  $U_C$  for (a) the coil mounting device approximately 2 cm displaced from the centre of the gantry, (b) the displacement reduced by 1 cm and (c) the coil mounting device in the middle of the gantry. Depending on the position, either  $U_R$  or  $U_C$  has a bigger amplitude, therefore, at a certain position (approximately met in (b)), full compensation is theoretically achievable. Notice that no probe is inserted into the scanner, the signal is solely generated by the Drive Field.

The voltage  $U_C$  in the CC changes noticeably when shifting the coil mounting device, while  $U_R$  in the RC stays constant, in accordance with the simulation studies in [Section 2.3](#).

In Fig. 23b, both voltages have the same amplitude, therefore, they are now superimposed with a  $180^\circ$ -phase shift and the resulting voltage is measured (Fig. 24).

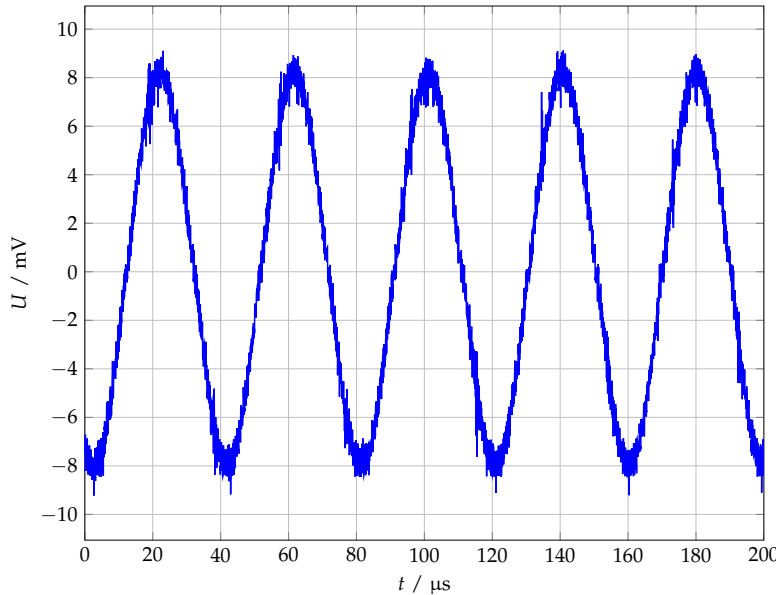


Figure 24: Compensated signal of the Drive Field. A reduction of 55.61 dB has been achieved.

As expected, the superposition of the voltages does not yield a complete compensation even though they have the same amplitude. Shifting the coil mounting device in either direction shows that the measured voltage is the minimum value of the superposition. The phase shift due to the parasitic capacitances described in [Section 2.3.2](#) renders a complete compensation impossible. Therefore, one has to find a mean to equalise the phases.

### 3.2 THE PHASE SHIFT

The simulation and the measurement of the Inductive Decoupling method above both show a phase shift between the two voltage signals  $U_R$  and  $U_C$ . A mathematical description of the problem is shown in Fig. 25: Complete compensation is only possible if the voltages are phase shifted by  $180^\circ$ . A deviation of only  $0.001^\circ$  would result in a maximum compensation of only up to a factor of  $10^{-5}$ , rendering the decoupling method insufficient. As the simulation studies in [Section 2.3](#) showed, this degree of phase shift is easily inherent in the system due to parasitic effects.

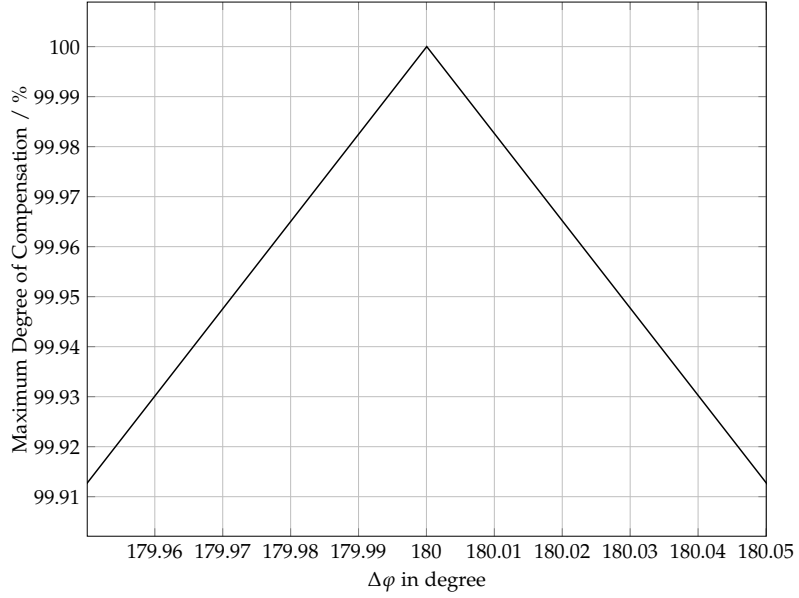


Figure 25: Phase difference  $\Delta\varphi$  between two signals and the resulting maximal compensation.

In order to calculate the phase shift, one first needs the frequency of the DF signal. This is calculated by fitting a quadratic function  $y = p_0 + p_1x + p_2x^2$  to the first and the last maximum of  $U_R$  in Fig. 30a and dividing the acquired time difference by 4. Fig. 26 shows the quadratic fit and its residuals for the first maximum.

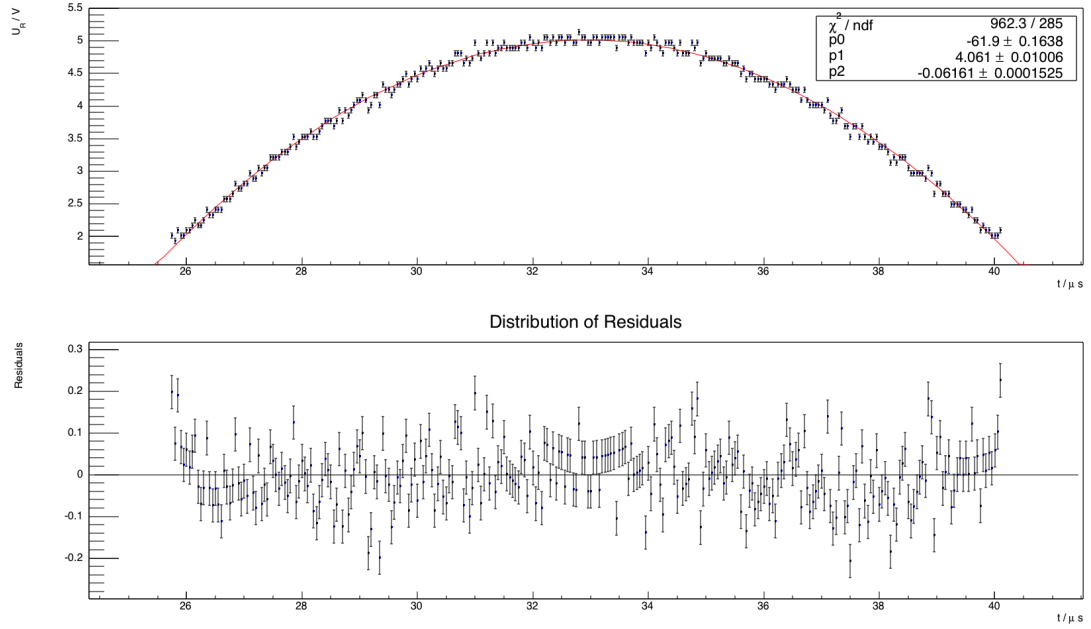


Figure 26: Quadratic fit of  $y = p_0 + p_1x + p_2x^2$  to first maximum of  $U_R$  measurement in order to determine the frequency of the Drive Field signal. The residuals show a systematic due to the limited voltage resolution of the oscilloscope.

The uncertainty on each voltage measurement is determined by the 8 bit resolution of the oscilloscope, while the error on the time measurement is given by the 500 GS/s

sampling rate [16]. The residuals show systematics due to the binning of the voltage values by the oscilloscope.

The calculated frequency is  $f = (26077 \pm 27)$  Hz.

The phase shift for any measurement is then determined by performing a linear regression of  $y = p_0 + p_1x$  on the first zero crossing of each voltage and plugging the acquired time difference into Equ. 8. The fitted time range is chosen to be in accordance to the small-angle approximation of  $10^\circ$ . An exemplary fit is shown in Fig. 27.

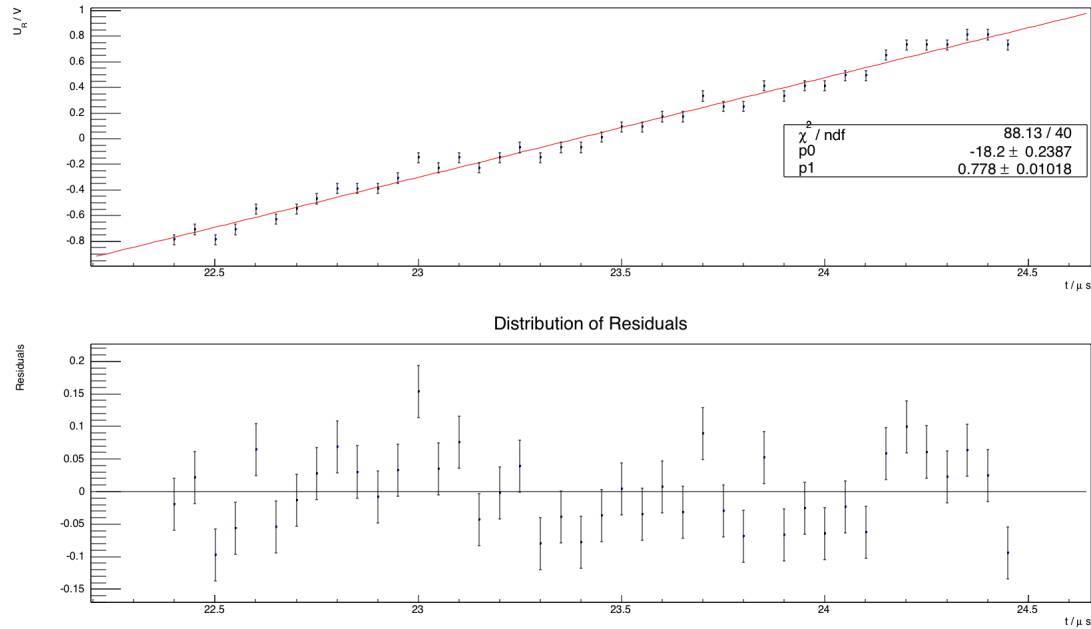


Figure 27: Linear regression of  $y = p_0 + p_1x$  to first zero crossing of  $U_R$  measurement in order to determine the phase shift to  $U_C$  in Fig. 30a.

Getting back to the phase equalising problem, the easiest solution to this problem would be using two identical coils. As this is only achievable to a certain degree in practice, an alternative solution is to use an electronic circuit made of components with different reactances, e.g. an inductor  $L$  and a resistor  $R$ . Designing a voltage divider with these components results in a frequency-dependent phase shift of the output voltage.

If the phase shift is small enough, one could also delay one voltage signal using a piece of copper wire. With the velocity factor  $VF = 0.951$  of copper wire[15], the length of wire needed to delay a 26 kHz signal resulting in a  $0.01^\circ$  phase shift is

$$l = \frac{VF \cdot c}{f} \cdot \frac{1}{36000} = 0.31 \text{ m.} \quad (17)$$

### 3.2.1 Allpass-Filter

The *allpass-filter* (AF) is a voltage divider as described above. It consists of three resistors and a capacitor (Fig. 28).

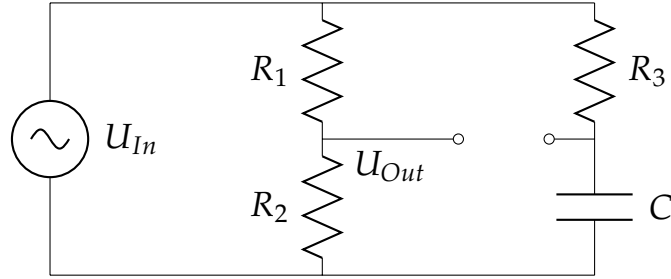


Figure 28: Circuit diagram of the allpass-filter

The ratio of the input and the output voltages shows that the achieved phase shift is solely dependent on the values of  $R_3$  and  $C$  [17]:

$$\frac{U_{Out}}{U_{In}} = \frac{R_1 - \omega^2 R_2 R_3^2 C^2}{(R_1 + R_2) \cdot (1 + \omega^2 R_3^2 C^2)} - \frac{i}{\omega R_3 C + \frac{1}{\omega R_3 C}} \quad (18)$$

Therefore, by providing the input voltage with either the RC or the CC, it is possible to adjust the phase shifts between the Receive and Compensation signals. An LTSpice simulation shows the desired effect (Fig. 29).

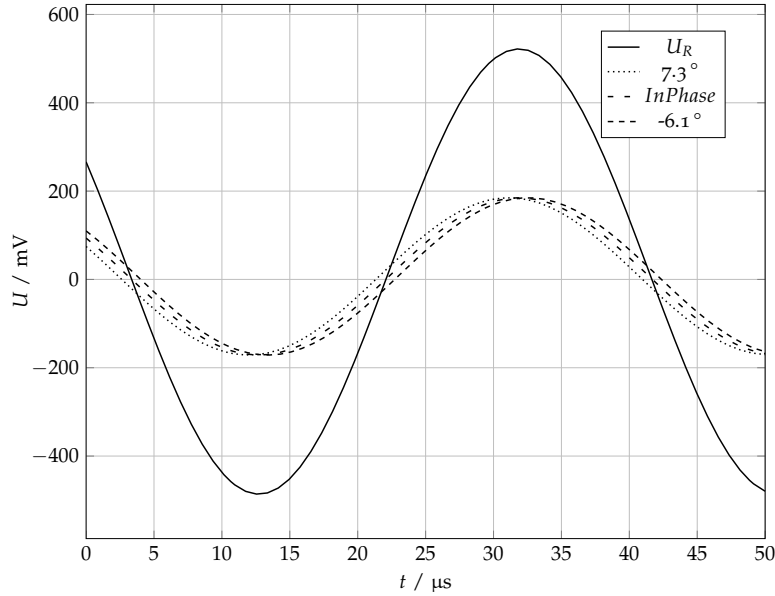


Figure 29: LTSpice simulation showing the effect of an allpass-filter.  $U_R$  is the simulated voltage in the Receive Coil. The densely dashed line is the voltage  $U_C$  in the Cancellation Coil, phase shifted by  $7.3^\circ$ . By increasing the capacitance of  $C$  the phase shift is corrected until it is in phase (loosely dashed line). Increasing the capacitance further results in overcompensation (dashed line).

Here,  $R_1$  was chosen to be equal to  $R_2$ , therefore the amplitude of  $U_C$  is reduced by half. The simulation shows that using a variable capacitor is advantageous as one can equalise a range of phase shifts with the same AF.

In order to test this method, an AF with the following components is built (Tab. 5).

COMPONENT	$C / pF$	$Z / \Omega$	$L / \mu H$
$R_1$	-	$10.01 \pm 0.02$	$0.28 \pm 0.001$
$R_2$	-	$9.98 \pm 0.02$	$0.26 \pm 0.001$
$R_3$	-	$2.97k \pm 6$	$250 \pm 0.5$
$C$	$11.17 \pm 0.02 - 121.96 \pm 0.24$	$15.3 \pm 0.03$	-

Table 5: Measured component values of the allpass-filter used in the following experiments.

An LTSpice simulation shows that the range in capacitance of  $C$  enables a phase shift change between  $0.6^\circ$  and  $5.5^\circ$ .

Exemplary results and the calculated phase shifts are shown in Fig. 30. A positive phase shift means that the phase angle of  $U_R$  is bigger than the one of  $U_C$ .

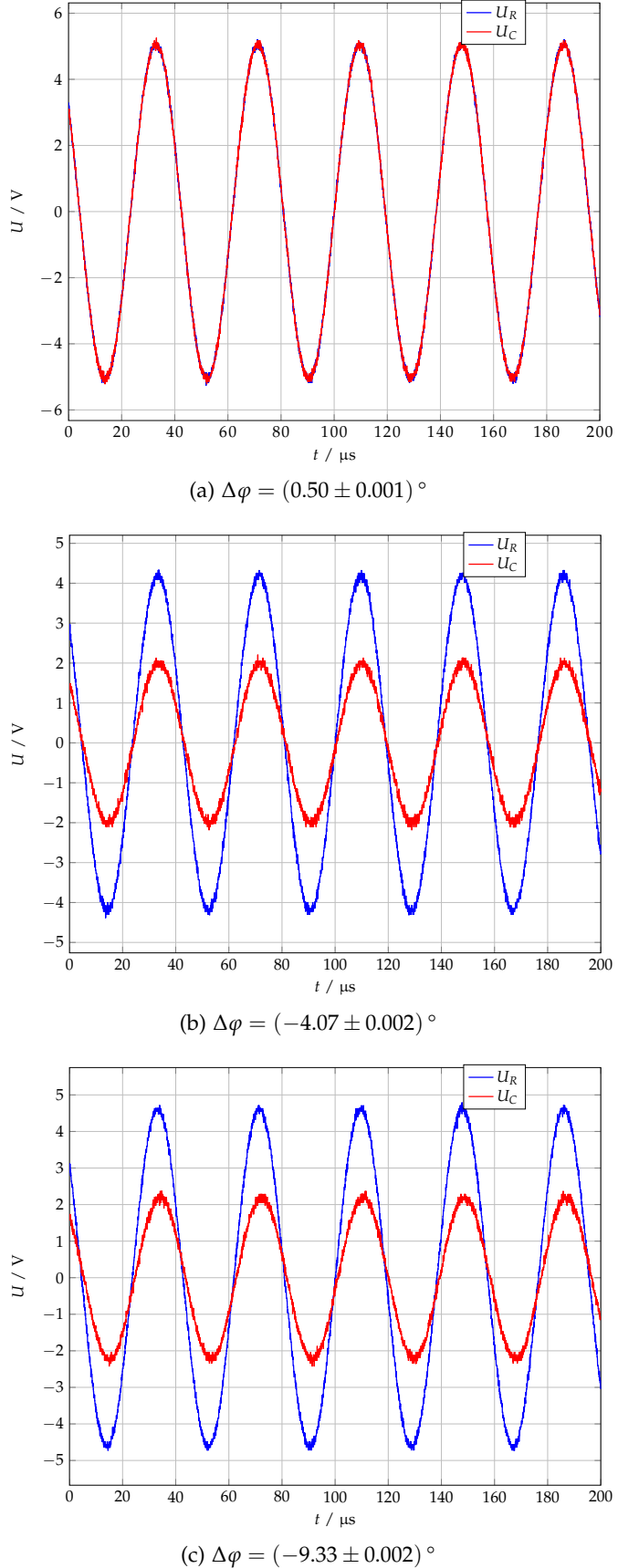


Figure 30: The voltages induced by the Drive Field in the Receive Coil  $U_R$  and the Cancellation Coil  $U_C$  (a) without an allpass-filter, (b) with an allpass-filter ( $C = (11.24 \pm 0.02)$  pF) attached to the Cancellation Coil, (c) with an allpass-filter attached to the Cancellation Coil and a varied capacitance ( $C = (120.84 \pm 0.24)$  pF) in comparison to (b).

The measurements show that the AF can be used to alter the phase shift between the  $U_R$  and the  $U_C$ . The range of available phase shift is between  $-4.07^\circ$  and  $-9.33^\circ$ , and therefore a bit more than the simulated range of  $4.9^\circ$ , most likely due to the uncertainties on the measured component values of the AF.

There is an additional phase shift of about  $3.9^\circ$  caused by the parasitic inductances in the AF circuit. Unfortunately, this additional phase shift means that for this pair of RC and CC, the AF does not yield a further compensation.

A gain in compensation is achieved in the next measurement. Fig. 31 shows the DF signal in the RC and the CC.

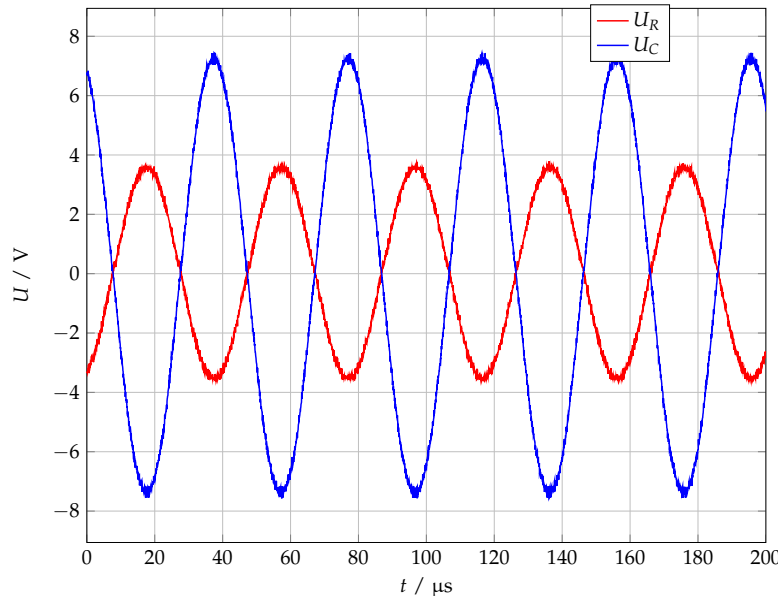


Figure 31: Drive Field induced voltages in the Receive and the Cancellation Coil. The parasitic phase shift is  $\Delta\varphi = (7.73 \pm 0.002)$ .

Next, the signals are superimposed and the AF is connected in between. Fig. 32 shows the resulting compensated signal for three different capacitance values.

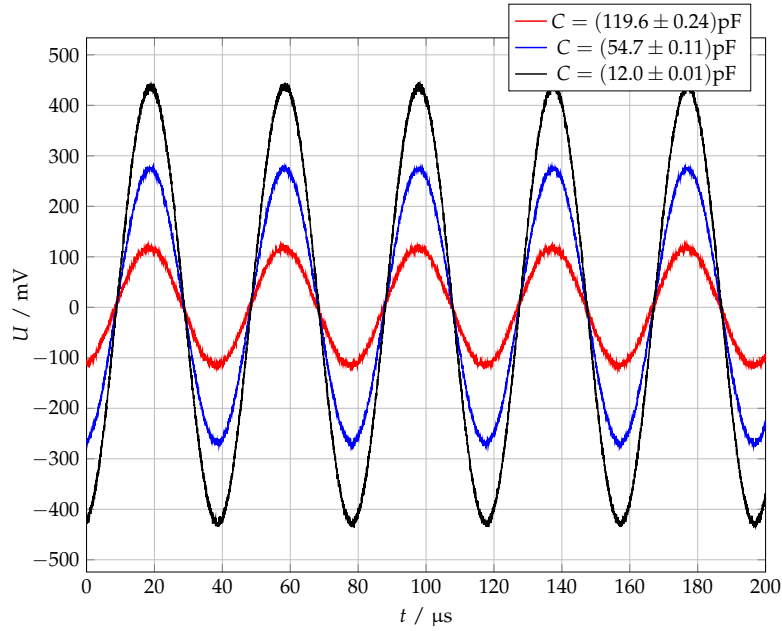


Figure 32: The compensated signal of the voltages shown in Fig. 30 for three different capacitance values of the allpass-filter. By varying the phase shift between the voltages in the Receive and the Cancellation Coil different degrees of compensation are achieved.

By further adjusting the position of the coil mounting device, the minimum value of the compensated signal is measured (Fig. 33).

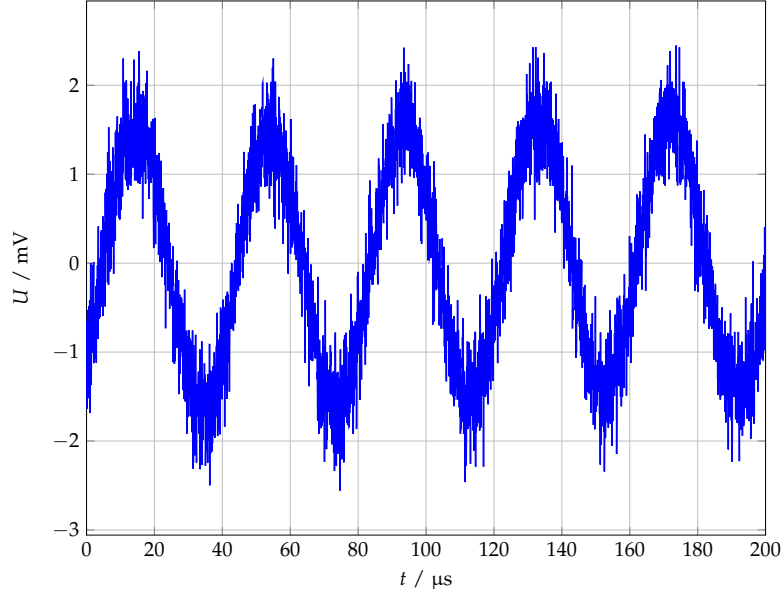


Figure 33: The maximum degree of compensation achieved by use of an allpass-filter. Extrinsic noise voltage is clearly visible in this order of magnitude. A reduction of about 66.47 dB has been achieved.

These results show that the AF can improve the compensation by adjusting the phase shift. However, complete phase equalisation and therefore full compensation

has not been achieved. Performing measurements with the allpass-filter proved to be challenging as the circuit heated up noticeably, indicating an unexpected current flow in the receive signal chain. This shows that the performed simulation studies of the AF were not sufficient and need to be improved for further application.

In addition, a noise calculation of the used AF yields 7.05 nV, three orders-of-magnitude higher than the coil noises, due to the resistance value of  $R_3 = 3 \text{ k}\Omega$ . It therefore is necessary to move on to a different layout of the AF, presented in the next section.

### 3.2.2 Outlook: Lattice Phase Equaliser

The *lattice phase equaliser* (LPE) is an allpass-filter made of purely reactive components, yielding a vanishing resistance. The circuit diagram is shown in Fig. 34 [18].

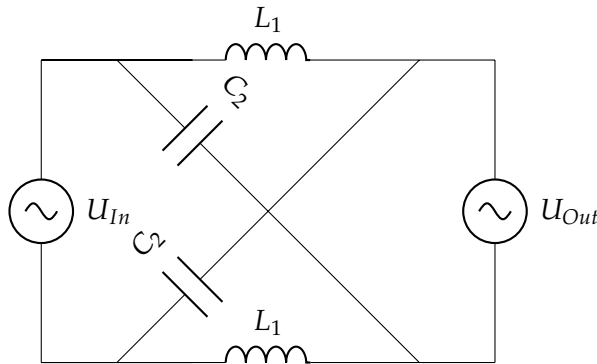


Figure 34: Circuit diagram of the lattice phase equaliser

The phase shift between  $U_{In}$  and  $U_{Out}$  is caused by the different frequency dependencies of the reactances of the inductors and capacitors. The elements with the inductors  $L_1$  are called the series elements, while the ones with the capacitors  $C_2$  are the lattice elements. If the impedances are chosen to be the dual of each other, i.e.

$$\frac{Z_L}{Z_0} = \frac{Z_0}{Z_C}, \quad (19)$$

with  $Z_0$  being the characteristic impedance of the LPE, then the circuit results in a constant resistance network, i.e. the attenuation is independent of the frequency. The phase shift is then given by

$$\tan\left(\frac{\Delta\varphi}{2}\right) = \frac{-X_L}{Z_0}, \quad (20)$$

with

$$\begin{aligned} Z_L &= iX_L \\ &= i2\pi f L, \end{aligned} \quad (21)$$

where  $L$  is the inductance of  $L_1$  and  $f$  is the voltage frequency [18]. There have not been any experiments conducted with the LPE, however, it promises to equalise the phases without decreasing the SNR significantly.



## CONCLUSION AND OUTLOOK

---

The work presented in this thesis shows that Inductive Decoupling is a sound method to compensate the Drive Field feedthrough interference in MPI. The performed simulation studies present means to construct a coil topology which is least susceptible to errors in area and position deviation of the Receive or the Cancellation Coil. In addition, the LTSpice circuit simulations highlight that the parasitic quantities of the coils yield a crucial phase shift. While the proposed set-up of the allpass-filter did improve the compensation, the noise calculation showed that it is not suitable for MPI, and another mean to adjust the phases was introduced, the lattice phase equalizer.

While the achieved degree of compensation is three orders of magnitude too low to be sufficient for application yet, the simulation studies illustrate the potential Inductive Decoupling has and the measurements using an allpass-filter are a promising start. In order to continue this work and enhance decoupling, several approaches can be extracted from the previous chapters:

- Further fine tuning of the coil mounting device can reduce the error proneness, while enhancing compensation by better adjusting the Receive Coil and the Cancellation Coil to one another. In addition, after acquiring detailed data about the magnetic field in the gantry, the simulations themselves can be improved. This characterisation of the magnetic field is currently under progress at the *Department for Experimental Molecular Imaging* at the RWTH Aachen.
- Once the magnetic field is characterised and the best layout for the Receive and the Cancellation Coil is calculated, the components of the allpass-filter can be chosen to reduce parasitic effects and equalise the phase shift.
- In order to decrease the noise introduced to the system by the Cancellation Coil, it could be connected in parallel to a capacitor, forming a resonator circuit.
- As it has been suggested by Graeser et al. [5], one could combine a band-stop filter and a Cancellation Coil to achieve an overall signal in the dynamic range of the used ADC.



## BIBLIOGRAPHY

---

- [1] B. Gleich, J. Weizenecker, *Tomographic imaging using the nonlinear response of magnetic particles*. Nature **435**, June 2005
- [2] T. Knopp, T. M. Buzug, *Magnetic Particle Imaging*. Springer-Verlag Berlin Heidelberg, 2012
- [3] R. P. Feynman, R. B. Leighton, M. Sands, *The Feynman Lectures on Physics*, Vol.II, Addison-Wesley, 1964.
- [4] Emine U. Saritas , Patrick W. Goodwill, Laura R. Croft, Justin J. Konkle, Kuan Lu, Bo Zheng, Steven M. Conolly, *Magnetic Particle Imaging (MPI) for NMR and MRI researchers*. Journal of Magnetic Resonance, 2013.
- [5] M. Graeser, T. Knopp, M. Grüttner, T. Sattel, T. M. Buzug, *Analog receive signal processing for magnetic particle imaging*. Medical Physics, Vol. 40, 2013
- [6] V. Schulz, M. Mahlke, S. Hubertus, F. Kiessling, M. Straub, *Towards a holistic MPI signal detection using a field cancelation local receive coil topology*. Transactions on Magnetics - Conferences , 2014.
- [7] J. Weizenecker, J. Borgert, B. Gleich, J. Rahmer, H. Dahnke, *Three-dimensional real time in vivo magnetic particle imaging*, Physics in Medicine and Biology, Issue 54, 2009
- [8] J. Franke, U. Heinen, L. Matthies, V. Niemann, F. Jaspard, M. Heidenreich, T. Buzug, *First hybrid MPI-MRI imaging system as integrated design for mice and rats: Description of the Instrumentation Setup*, IWMPI 2013 Conference Record, 2013.
- [9] Patrick Vogel, Martin A. Rückert, Walter H. Kullmann, Peter M. Jakob, Volker C. Behr, *Slice Scanning Mode for Travelling Wave MPI*, International Workshop on MPI, 2013
- [10] S. Hubertus, *Investigation on Image Resolution Improvement Technologies for Magnetic Particle Imaging*, Bachelor Thesis, 2014
- [11] F. Neumann, *Allgemeine Gesetze der inducirten elektrischen Ströme*. Abhandlungen der Königlichen Akademie der Wissenschaften zu Berlin, 1847
- [12] Agilent Technologies, *Agilent U1731C, U1732C and U1733C Handheld LCR Meter*, Retrieved August 28, 2014, from <http://cp.literature.agilent.com/litweb/pdf/U1731-90077.pdf>
- [13] G. Vasilescu, *Electronic Noise and Interfering Signals*. Springer Berlin Heidelberg New York, 2005
- [14] H. Nyquist, *Thermal Agitation of Electric Charge in Conductors*. Physical Review Vol. 32, Pages 110-113, 1928

- [15] Air Stream, *Calculating the length of an Antenna*, Retrieved September 3, 2014, from <http://www.air-stream.org.au/technical/calculating-length-antenna>
- [16] Tektronix, *Mixed-Signal-Oszilloskope MSO4000B/DPO4000B-Serien Datenblatt*, Retrieved September 6, 2014, from [http://de.tek.com/sites/tek.com/files/media/media/resources/MSO4000-DPO4000-Datasheet-DE-DE\\_3GG-20156-16\\_0.pdf](http://de.tek.com/sites/tek.com/files/media/media/resources/MSO4000-DPO4000-Datasheet-DE-DE_3GG-20156-16_0.pdf)
- [17] D. Mietke, *Allpassfilter*, Retrieved August 20, 2014, from <http://elektroniktutor.oszkim.de/analogtechnik/allpass.html>
- [18] O.J. Zobel, *Phase-shifting network*, US patent 1 792 523, filed 12 March 1927, issued 17 Feb 1931.

## DECLARATION

---

I, Max Mahlke, hereby certify that this document has been composed by myself, and describes my own work, unless otherwise acknowledged in the text.

*Aachen, September 2014*

---

Max Mahlke, September 11, 2014

## ACKNOWLEDGEMENTS

---

My work has benefited greatly from the support I have received in the last few months. Especially the following people were a never ending source of advice and help.

First and foremost, I would like to thank the Royal Philips N.V. for providing the MPI scanner to the RWTH Aachen University and for giving me the opportunity to write my thesis on it.

In addition, I would like to express my gratitude to Professor Volkmar Schulz for supervising my work and for his valuable assistance throughout the process, as well as to Professor Achim Stahl for supervising my work as well.

Marcel Straub has my deepest thanks for his constant advice and for his patience with me, for proof reading and, especially, for teaching me over and over again.

On a final note, I would like to thank B.Sc. Simon Hubertus for the discussion we had, the laughs we shared and for sometimes knowing my topic better than me. And, of course, for proof reading.